Optical properties and oxidative potential of aqueous-phase products from OH and $^3C^*$-initiated photolysis of eugenol

Xudong Li[1], Ye Tao[1], Longwei Zhu[1], Shuaishuai Ma[1], Shipeng Luo[1], Zhuzi Zhao[1], Ning Sun[1], Xinlei Ge[2,*], Zhaolian Ye[1,*]

[1]College of Chemistry and Environmental Engineering, Jiangsu University of Technology, Changzhou 213001, China

[2]Jiangsu Key Laboratory of Atmospheric Environment Monitoring and Pollution Control, Collaborative Innovation Center of Atmospheric Environment and Equipment Technology, School of Environmental Sciences and Engineering, Nanjing University of Information Science and Technology, Nanjing 210044, China

*Correspondence: Zhaolian Ye (bess_ye@jsut.edu.cn) and Xinlei Ge (caxinra@163.com)

Abstract: Aqueous reactions may turn precursors into more light-absorbing and toxic products, leading to air quality deterioration and adverse health effects. In this study, we investigated eugenol degradation in the aqueous phase by direct photolysis, and indirect photooxidation in the presence of radicals (triplet excited state ($^3C^*$) and hydroxyl radical (•OH)). Results showed degradation rates of eugenol followed the order of $^3C^*$>•OH >direct photolysis. Relative contributions of reactive oxygen species (ROS) were evaluated via combination of radical quenching tests, deoxygenated experiments and electron spin resonance (ESR) method, and results showed that $^3C^*$ played a dominant role in eugenol degradation for $^3C^*$-initiated oxidation, while $O_2^{•-}$ generated were important for OH-initiated oxidation. Rate constants under O_2, air and

N2 followed the order of $k_{O_2} > k_{Air} > k_{N_2}$ for both direct photolysis and OH-initiated

oxidation, and it changed to $k_{Air} > k_{N_2} > k_{O_2}$ for $^3C^*$-initiated oxidation. UV-vis

absorption spectra showed absorbance enhancement in the 300-400 nm range after

photooxidation, and new fluorescent spectra at excitation/emission=250/400-500 nm

appeared, suggesting the formation of new chromophores and fluorophores, such as

humic-like substances (HULIS). Concentration of generated HULIS first increased

gradually then leveled off over time. Dithiothreitol assay was applied to assess

oxidation potential of products, which was greater than that of eugenol, suggesting

more harmful species were produced during oxidation. The carbon oxidation state and

oxygen-to-carbon ratio from aerosol mass spectrometry both increased with time,

indicating that SOA became more oxidized. Detailed reaction pathways were elucidated

via analyses of chemical characteristics of the products.

1 Introduction

Photochemical reactions in atmospheric aqueous phase (cloud droplet, fog droplet

and aerosol water) affect the lifetimes of many organic species, and are important

sources and aging pathway of secondary organic aerosol (SOA) (Vione et al., 2006;

Zhao et al., 2012). Different from the gasSOA formed through gas-phase photochemical

oxidation, aqueous-phase SOA (aqSOA) typically is usually more oxidized and less

volatile, so it plays an important role in haze formation, air quality and global climate

change (Ervens et al., 2011; Lim et al., 2010). However, due to complexity of reaction

mechanisms and control factors (such as precursors, oxidants, and light source), there

are still many unknowns regarding aqueous reactions. For example, reaction

mechanism, optical property, oxidative potential (OP) and relations between them

49   remain poorly understood.

50   Most laboratory studies so far have focused on aqueous-phase oxidation of small

51   molecular weight VOCs, such as isoprene, terpenes (α-pinene and β-pinene), as well as

52   their gas-phase oxidation products (such as glyoxal, methylglyoxal, *cis*-pinonic acid

53   and methyl vinyl ketone) (Faust et al., 2017; Herrmann, 2003; Herrmann et al., 2015;

54   Huang et al., 2011; Lee et al., 2012; Zhang et al., 2010). Now concerns have been

55   extended to semi-/intermediate volatility VOCs (S/IVOCs), especially phenolic

56   compounds, which could be produced by combustion or pyrolysis of lignin in biomass

57   (Barzaghi and Herrmann, 2002; Bonin et al., 2007; Chen et al., 2020; Gilardoni et al.,

58   2016; He et al., 2019; Jiang et al., 2021; Li et al., 2014; Li et al, 2021; Ma et al.,

59   2021;Mabato et al., 2022; Smith et al., 2014; Sun et al., 2010; Tang et al., 2020; Yang

60   et al., 2021; Yu et al., 2016). Generally, chemical structure of precursors has profound

61   influence on aqSOA and reaction mechanisms, however, the effect of oxidant on SOA

62   formation also cannot be neglected. It is evident that liquid water contains many

63   oxidants, such as singlet oxygen ($^1O_2$), nitrate radical (NO_3), hydroxyl radical (•OH),

64   and organic triplet excited states ($^3C^*$), which play crucial roles in photochemical

65   oxidation reactions (Kaur and Anastasio, 2018; Scharko et al., 2014). Among them,

66   •OH is the ubiquitous oxidant in atmospheric condensed phase, with concentration of

67   10^{-13}-10^{-12} mol·L^{-1} (Arakaki et al., 2013; Gligorovski et al., 2015; Herrmann et al.,

68   2003). Hence, aqueous-phase •OH-induced photodegradation has been extensively

69   studied (Chen et al., 2020; Sun et al., 2010; Yu et al., 2016). Compared to •OH oxidation,

70    $^3C^*$-initiated aqueous-phase reaction (photosensitized reaction) has also attracted

71   attention in recent years (Ma et al., 2021; Wang et al., 2021). Several classes of organic

72   compounds in the atmosphere, including non-phenolic aromatic carbonyls, quinones,

73   aromatic ketones and nitrogen-containing heterocyclic compounds, can form $^3C^*$ after

74 absorbing light (Alegría et al., 1999; Kaur et al., 2019; Nau and Scaiano, 1996;

75 Rossignol et al., 2014). These compounds are termed photosensitizers. $^3C^*$ is capable

76 of reacting with O_2 to produce singlet oxygen ($^1O_2$) and superoxide radicals ($O_2^{\bullet-}$).

77 Various reactive oxygen species (ROS) can be generated and play a critical role in $^3C^*$-

78 initiated aqueous-phase reactions. Despite strong evidence in support of the importance

79 of ROS in photochemical process (Ma et al, 2021;Wang et al., 2020; Wang et al., 2021;

80 Wu et al., 2021), however, our understanding on $^3C^*$-initiated SOA is still limited.

81 Excitation emission matrix (EEM) fluorescent spectroscopy, as a low-cost, rapid,

82 non-destructive and high-sensitivity technique, can offer detailed information on

83 chromophores hence has been widely employed for studies of aquatic dissolved organic

84 matter (Aryal et al., 2015). Nevertheless, it has not been extensively used in

85 atmospheric aerosol research (Mladenov et al., 2011). Several recent studies have

86 investigated the relationship between the fluorescence components and chemical

87 structures of atmospheric aerosols through combining high-resolution aerosol mass

88 spectrometry (AMS) and EEM fluorescent spectroscopy (Chen et al., 2016a; Chen et

89 al., 2016b). Earlier report from Chang and Thompson (2010) found fluorescence

90 spectra of reaction products during aqueous reaction of phenolic compounds, with some

91 similarities with fluorescence characteristics of humic-like substances (HULIS).

92 Subsequently, numerous studies have observed light-absorbing products formed in

93 aqueous photodegradation and further verified that aqueous reaction was a potential

94 source of HULIS (Li et al., 2021; Smith et al., 2016; Tang et al., 2020). Recently, Li et

95 al. (2021) began to apply EEM technique to characterize formation of light-absorbing

96 compounds in aqueous-phase oxidation of syringic acid. Additionally, studies (Chang

97 and Thompson, 2010) showed that light-absorbing and fluorescent substances generally

98 have large conjugated moieties (i.e., quinones, HULIS, polycyclic aromatic

99 hydrocarbons (PAHs)), which can damage human body (Dou et al., 2015; McWhinney

100 et al., 2013). HULIS are considered as an important contributor to induce oxidative

101 stress since they can serve as electron carriers to catalyze ROS formation (Dou et al.,

102 2015; Ma et al., 2019; Huo et al., 2021; Xu et al., 2020), causing adverse health effect.

103 Dithiothreitol (DTT) assay (Alam et al., 2013; Chen et al., 2021; Verma et al., 2015a),

104 as a non-cellular method, was widely employed to determine oxidation activity and

105 assess oxidative potential of atmospheric PM via the rate of DTT consumption (Chen

106 et al., 2019; Cho et al., 2005), since oxidative stress was related to adverse health effect.

107 Some other works (Fang et al., 2016; McWhinney et al., 2013; Verma et al., 2015;

108 Zhang et al., 2022) focused on the link between chemical composition and OP in PM,

109 and have confirmed that several kinds of compounds, such as quinones, HULIS and

110 transition metals usually have strong DTT activities. However, to the best of our

111 knowledge, DTT method has not been applied to evaluate the OP of aqueous-phase

112 oxidation products up to now.

113   In the present work, we choose 4-allyguaiacol/eugenol, as a model compound to

114 conduct aqueous phase reaction. As a representative methoxyphenol emitted from

115 biomass burning (Hawthorne et al., 1989; Simpson et al., 2005), it was widely detected

116 in atmospheric particles. For instance, emission concentration and factor emitted from

117 beech stove were 0.032 μg/m^3 and 1.534 μg/g, which are twice of those of (0.016 μg/m^3

118 and 0.762 μg/g) guaiacol (Bari et al., 2009; Liu et al., 2019). Eugenol is a representative

119 semivolatile aromatic compounds with moderate water-solubility (2.46 g/L at 298 K).

120   The characteristics of products were statistically elucidated by combining results

121 from high-performance liquid chromatography (HPLC), ultraviolet and visible (UV-

122 Vis) spectrophotometry, gas chromatography mass spectrometry (GC-MS), EEM and

123 soot-particle aerosol mass spectrometer (SP-AMS). The relative importance of various

ROS species to eugenol degradation was explored in order to clarify reaction mechanism. This study also investigated the light-absorption, fluorescent and oxidative properties of the aqueous oxidation products. Comparison on product properties under direct photolysis (without oxidant) and oxidation by •OH and $^3C^*$ were carried out.

2 Materials and methods

2.1 Chemicals and reagents

Eugenol (99%), tert-butanol (TBA, 99%), 3,4-dimethoxybenzaldehyde (DMB, 99%), para-benzoquinone (*p*-BQ, 99%), dithiothreitol (99%) and 5,5′-dithiobis-2-nitrobenzoic acid (DTNB, 99%), 2-nitro-5-thiobenzoic (99%) and 2,2,6,6-tetramethylpiperidine(TEMP) were all purchased from Sigma-Aldrich chemical company. Superoxide dismutase (SOD) was from Bovine Erythrocytes BioChemika. Dichloromethane (HPLC-MS grade, 99%), methanol (HPLC-MS grade, 99%), acetonitrile (HPLC-MS grade, 98%), H_2O_2 (35 wt. %), and 2,4,6-trimethylphenol (TMP, 99%) were all obtained from Acors Chemicals. Sodium azide (NaN$_3$, 98%) was purchased from J&K Scientific Ltd. (Beijing, China). All solutions were prepared using ultrapure water (Millipore) on the day of experiments.

2.2 Photochemical experiment

Aqueous phase photochemical reactions were carried out in a Rayonet photoreactor (model RPR-200), equipped with 16 light tubes (equipped with 2 RPR-3000, 7 RPR-3500 and 7 RPR-4190), which was frequently used for photochemical reaction and described in detail by several groups (George et al., 2015; Hong et al., 2015; Huang et al., 2018; Jiang et al., 2021; Zhao et al., 2014) to mimic sunlight. Pyrex

tubes containing sample solution were placed in the central and received radiation from

surrounded lamps from all sides. To ensure mixing of the solution, a fan and a magnetic

stir bar are placed at the bottom of solution. The solution temperature was controlled at

$25\pm2°C$. The photoreactor system was the same as above-mentioned and normalized

distribution of the photon fluxes inside RPR-200 illumination system have been

reported elsewhere (George et al., 2015). According to previous description, the

wavelength of photon fluxes was over 280 and 500 nm range. In this work, we only

measured light intensity at the surface of the reaction solution with a radiometer

(Photoelectric instrument factory of Everfine Corporation, Hangzhou, China). The light

intensity in the range of 290-320 nm (UVB) was ~2400 $\mu W/cm^2$, which was lower than

sunlight intensity (6257.1 $\mu W/cm^2$).

In this work, 300 μM H_2O_2 and 15 μM DMB were added into solution as sources

of •OH and $^3C^*$ radicals, respectively. The initial concentrations of eugenol was applied

as 300 μM. For $^3C^*$-mediated experiment, solutions were adjusted to pH=3 by sulfuric

acid in order to perform experiments under optimal conditions (Ma et al., 2021; Smith

et al., 2014) since DMB triplet state is protonated to a more reactive form in acidic

solutions. We conducted three sets of photolysis experiments: (A) 300 μM eugenol+300

μM H_2O_2; (B) 300 μM eugenol+15 μM DMB; and (C) 300 μM eugenol. In each series

of photochemical oxidation, a dark control experiments was done synchronously with

a Pyrex tubes wrapped by aluminum foil. The control results showed the loss of eugenol

under dark reaction could be negligible (data not shown). In addition, to evaluate the

role of ROS to eugenol degradation in $^3C^*$-initiated oxidation process, quenching

experiments using specific scavengers to trapping produced ROS were performed, such

as TBA for •OH, NaN_3 for $^1O_2$, SOD for $O_2^{•-}$, and TMP for $^3C^*$, respectively (Pan et al.,

2020; Wu et al., 2021). In •OH-initiated oxidation process, quenching experiments

171   using *p*-BQ for $O_2^{\bullet-}$ (Ma et al., 2019; Raja et al., 2005), and TBA for •OH were

172   conducted. For most series of experiments, solution was saturated by air and all

173   experiments presented were conducted in triplicate unless otherwise stated. The results

174   were shown in respect of average plus/minus standard deviation. In order to further

175   evaluate the role of oxygen in the photodegradation, experiment were also conducted

176   under different saturated gas (air, N_2 and O_2).

177   **2.3 Analytical methods**

178   **2.3.1 Determination of eugenol concentration**

179   Before and during photochemical reaction, 2 mL of reacted and controlled

180   solutions were sampled periodically and subjected to HPLC (LC-10AT, Shimadzu,

181   Japan) to quantify the eugenol concentrations. HPLC was equipped with the

182   InertSustain AQ-C18 reverse phase column (4.6×250 mm, 5.0 μm, Shimadzu) and a

183   UV-vis detector. The mobile phase was a mixture of acetonitrile/H_2O (v/v: 60/40) at a

184   flow rate of 0.6 mL/min, and the detection wavelength was set at 280 nm. The first-

185   order kinetic rate constant of eugenol degradation can be obtained from the slope of

186   plot of -$\ln(c_t/c_0)$ versus reaction time as presented in Eq.(1).

187                            $\ln(c_t/c_0)=-kt$ (1)

188   Here,c_0 (μM) and c_t (μM) are eugenol concentration at the initial and reaction

189   time t; k stands for pseudo first-order rate constant.

190   **2.3.2 UV-vis and fluorescent spectra**

191   The UV-vis absorbance spectra of reacted solutions (placed in a 1 cm path length

192   quartz cuvette) were measured by using an UV-vis spectrophotometer (Specord 210

plus, Analytik Jenal., Germany). The instrument is a dual-beam optical system with tungsten and deuterium lamps as light sources. A reference absorption spectrum of ultrapure water was carried out in the same cuvette prior to sample analysis for baseline correction.

Immediately following UV-Vis measurement, the cuvette was transferred to a three-dimensional EEM fluorescence spectrometer (FluoroMax Plus,HORIBA Scientific) to record variation of fluorescence intensity upon irradiation. Spectral ranges varied from 200 to 450 nm for excitation wavelengths (Ex) and from 290-650 nm for emission wavelength (Em). Excitation and emission wavelength intervals were 5 nm and 2 nm steps, respectively. The reported absorbance and EEM spectra are the average of the results from triplicate experiments.

2.3.3 Determination of HULIS concentration

Solid phase extraction (SPE) cartridges (CNW Poly-Sery HLB, 60mg/cartridge) were used to isolate HULIS from the reaction solution. The original SPE cartridges was rinsed with 1 mL ultrapure water and 3 mL methanol prior to extraction. The solution was acidified to pH 2 using HCl and loaded on an SPE cartridge, subsequently rinsed with 1 mL ultrapure water. Next, 3 mL methanol-ammonia (98:2, v/v) was added into SPE cartridge to elute HULIS component, and was evaporated to full dryness with high-pure N_2, followed by dilution with ultrapure water to 25 mL for quantification of HULIS with HPLC coupled with an evaporative light scattering detector (ELSD3000). The recovery efficiency of standard SRFA was 75-80% and standard deviation of reproducibility test less than 5%. More details have been described elsewhere (Tao et al., 2021).

 2.3.4 Oxidative potential based on DTT assay

217   We detected OP based on previous DTT method (Cho et al., 2005; Lin and Yu,

218   2019) with minor improvements. Briefly, a 1.2 mL portion of sample solution was

219   transferred into 10 mL glass tube, then 6 mL phosphate buffer (0.1 M, pH 7.4) and 300

220   µL of 2.5 mM DTT were added and mixed thoroughly. The samples were placed in a

221   37°C water bath for incubation some time, and reaction was terminated at 30 min

222   intervals over the course of 150 min by taking 1 mL aliquots of DTT mixture and adding

223   100 µL of 5 mM DTNB (prepared in 0.1 mM phosphate buffer) to centrifuge tube. Next,

224   reaction between DTNB and DTT produced bright yellow TNB, which was quantified

225   using UV-Vis spectrometer within 30 min. Finally, we recorded light absorbance (A_t)

226   at 412 nm at time t to quantify indirectly remaining DTT. Another 1.2 mL ultrapure

227   water instead of sample solution was treated in the same way and absorbance was

228   denoted as A for distinguish from A_t. A_0 represents initial light absorbance value. Thus,

229   the concentration of DTT consumed by the sample solution (M_{DTT}, µM) and blank

230   solution (M_{DTT0}, µM) were calculated as Eq.(2) and Eq.(3), respectively.

231
$$M_{DTT} = \frac{A_0 - A_t}{A_0} \times C_{DTT_0} \tag{2}$$

232
$$M_{DTT0} = \frac{A_0 - A}{A_0} \times C_{DTT_0} \tag{3}$$

233   Here, C_{DTT0} was initial DTT concentration in sample solution (100 µM in this

234   work). DTT consumption rate (R_{DTT} and R_{DTT0}) was obtained from the slope of plot of

235   M_{DTT} and M_{DTT0} versus incubation time. Experiments of blanks and samples were

236   typically run in a triplicate. The reproducibility of the whole analysis showed that the

237   relative standard deviation of the DTT consumption rate analysis was 3-4%.

238   **2.3.5 Product analysis by GC-MS**

239   Reacted solution (about 30 mL) was extracted with 10 mL dichloromethane twice.

240   The extracts were concentrated to 1 mL using gentle N_2 blow drying, subsequently

241   transferred to a 2 mL vial, and analyzed with a GC-MS (7890A GC/5975C MS, Agilent),

242   using a DB-5ms capillary column (30 m×0.25 mm×0.5 μm). The operational conditions

243   were set as follows: injector at 200°C; ion source at 230 °C; The column oven

244   temperature was programmed: held at 35°C for 4 min, then ramped to 250 °C at a rate

245   of 20°C/min and held for 10 min. The recovery efficiency, method detection limits and

246   quality assurance/quality control has been described in detail elsewhere (Ye et al., 2020).

247   **2.3.6 SP-AMS analysis and aqSOA mass yield**

248   Aerodyne SP-AMS was applied to analyze low volatile organics in reaction

249   solution, similar to our previous work (Chen et al., 2020). AMS data were acquired in

250   V mode and analyzed by Squirrel v.1.56D and Pika v1.15D software. All the organic

251   fragment ions were classified into six groups: CH, CHO, CHN, CHO_2, CHON, HO.

252   Elemental ratios (O/C; hydrogen-to-carbon, H/C), were obtained according to the

253   method proposed by Canagaratna et al. (2015).

254   Since the AMS analysis requires the nebulization of sample solution into particles

255   before determination, and quantification of organics in each experimental run depend

256   on atomization efficiency and carrier gas flow, we cannot use SP-AMS recorded

257   concentration to quantify aqSOA mass directly. In this case, according to the method

258   suggested by Li et al. (2014), we added an internal standard (SO_4^{2-}) prior to AMS

259   analysis. The ratio of particle-phase organics to SO_4^{2-} ($\Delta Org/SO_4^{2-}$) after atomization

260   represented the relative aqSOA mass. Furthermore, aqSOA mass yield (Y_{SOA}, %),

261   which is generated aqSOA mass per unit mass of precursor consumed, can be calculated

262   as Eq. (4).

$$Y_{SOA}(\%) = \frac{(\Delta Org/SO_4^{2-})[SO_4^{2-}]_0}{C_0 M \eta} \times 100\% \qquad (4)$$

264 Where $[SO_4^{2-}]_0$ is the initially added SO_4^{2-} concentration (here 7.27 mg·L^{-1}); C_0 is

265 initial eugenol concentration, mmol/L; M is molecular weight of precursor (164 g/mol

266 for eugenol) , η is the degradation efficiency of eugenol.

3 Results and discussion

3.1 Kinetics of the photo-oxidation

269 Figure 1 shows unreacted eugenol concentrations (c_t) and the negative logarithm

270 of c_t/c_0 (-ln(c_t/c_0)) as a function of reaction time, respectively. The pseudo first-order

271 rate constant (k) obtained by Eq.(1) was also presented. Error bars represent one

272 standard deviation from triplicated measurements. As described in Figure 1a, eugenol

273 concentration decreased to be lower than 20% of the initial concentration at 3 h,

274 suggesting photolysis was fast under reaction conditions. In the presence of $^3C^*$,

275 eugenol was degraded to nearly 100% after 3 h. Previous study on 4-ethylguaiacol $^3C^*$-

276 initiated oxidation (Chen et al., 2020) showed that it degraded completely until 21 h.

277 Apart from difference of target precursor, different light irradiation spectra and stronger

278 energy of light sources in this work might be responsible for the fast loss of eugenol.

279 The BDEs are 340 kJ/mol for OH, 374 kJ/mol for C-H in -CH$_3$ group, 345 kJ/mol for

280 C-C in C=C bonds, and 403 kJ/mol for C-H in -OCH$_3$ group, respectively (Herrmann

281 et al., 2003; He et al., 2019). The lowest BDE was found for the O-H bond and C-C

282 bond. Due to the influence of steric hindrance and intramolecular hydrogen bonding,

283 the H-abstraction reaction from the OH group might have been less favorable. The most

284 favorable H-abstraction reaction might have taken place in the C-C in allyl group. As a

285 result of breakage of C=C into C-C at allyl group site, 2-methoxy-4-propyl-phenol

could form (see Section 3.6.1). As we known, when photon energy is higher than bond dissociation energy, they can directly break chemical bond of molecules, leading to decomposition of compounds and possibly further mineralization. The energies of photons at 300 and 350 nm in our light sources are 412 kJ/mol, and 353 kJ/mol, which are higher than the weakest BDEs in eugenol, as a result, eugenol molecule can directly absorb photo energy to decompose.

As shown in Fig. 1b, the first-order rate constants were 2.43×10^{-4} s^{-1}, 2.73×10^{-4} s^{-1}, and 5.75×10^{-4} s^{-1} for direct photolysis and photooxidation by •OH and $^3C^*$, respectively. $^3C^*$-initiated photodegradation was quicker than that with •OH due to contributions of combination of multiple pathways including reactions with $^1O_2$, $O_2^-\cdot$ and $\cdot OH$. A similar results were found for aqueous phase reaction of three phenols with •OH and $^3C^*$ by Yu et al. (2016) who showed degradation rates of three compounds were all higher with $^3C^*$ than •OH.
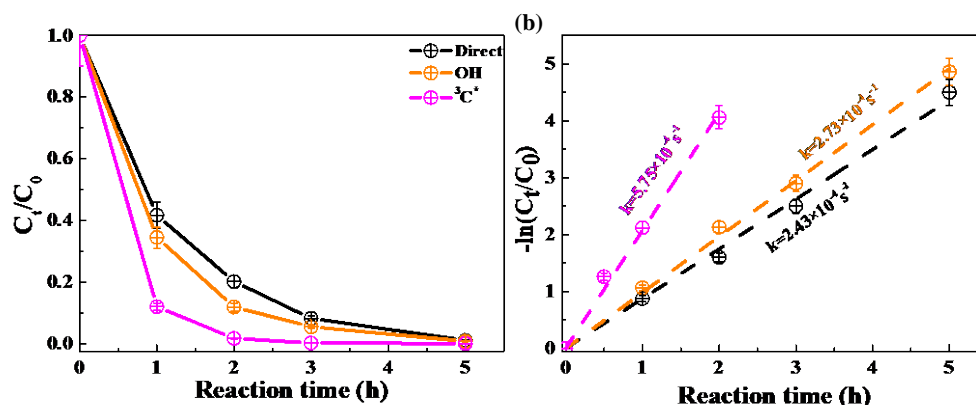
Figure 1. Aqueous phase eugenol decay kinetic curves (a) and rate constants (b) under three conditions. Error bars represent one standard deviation from replicated measurements.

3.2 Relative importance of ROS to photooxidation

3.2.1Quenching experiments in $^3C^*$-initiated photooxidation

304   Relative importance of ROS in photodegradation processes was usually

305   investigated by the addition of radical quenchers, and here it was calculated based on

306   the different degradation efficiencies of eugenol in absence and presence of different

307   ROS quenchers. For each scavenger, we conducted several gradient experiments with

308   varying molar ratios of eugenol to quenchers. The ratios were set as 0.075:1, 0.15:1,

309   0.3:1, 0.75:1, 1.5:1 for quenchers of NaN_3, TMP and TBA, and 1.2:1, 1.6:1, 2.5:1, 5:1,

310   10:1 for SOD, which were all within the typical range of molar ratios to quench ROS

311   reported previously (Zhou et al., 2018). Above concentrations of the added quencher

312   have been repeatedly adjusted to ensure the complete reactions between radicals and

313   scavengers. Figure 2 displays the effects of different ratios on eugenol degradation. As

314   shown, when adding quenchers into solution, all rate constants (k) were lower than

315   those of the quencher-free solutions. The optimum molar ratios of eugenol to quenchers

316   were selected when the inhibition degree of eugenol degradation unchanged with the

317   increase of added quencher mass (Wang et al., 2021). For example, upon decreasing

318   molar ratios of eugenol to NaN_3 from 1.5:1 to 0.075:1, the inhibitory degree of eugenol

319   degradation was unchanged at ratio of 0.15:1, indicating that $^1O_2$ has been absolutely

320   quenched at ratio of 0.15:1, so, we finally selected molar ratios of 0.15:1 for NaN_3,

321   since excess scavenger may produce other products that can change the existing

322   reaction. Finally, the molar ratios of eugenol to quencher TBA, NaN_3, TMP and SOD,

323   of 1.5, 0.15, 0.075 and 2.5 were selected, respectively. Table1 and Figure S1 compared

324   the rate constants determined under various radical quenchers and results showed that

325   the ranking of first-order rate constants were TMP<NaN_3<SOD<TBA, suggesting

326   relative importance of generated ROS to degradation was in the order of $^3C^*$＞$^1O_2$＞

327    $O_2^{\bullet-}$＞•OH. This result suggests that $^3C^*$ plays a major role in the photooxidation

328   reaction. Other studies (Laurentiis et al., 2013; Misovich et al., 2021) of aqueous DMB-

329   photosensitized reaction also showed $^3C^*$ was the greatest contributor to phenol or

330   guaiacyl acetone loss, followed by $^1O_2$, while both •OH and $^1O_2$ contributions were

331   relatively minor.

332   The value of $(k-k_{TMP})/k$ was 0.857, therefore contribution of $^3C^*$ was estimated to

333   be as high as 85.7%. In the same way, the contributions of $^1O_2$, $O_2^{•-}$ and •OH were

334   80.5%, 61.4% and 53.9%, respectively. The total contribution of the four ROS largely

335   exceeded 100%. This can be explained by the fact that ROS scavengers can actually

336   significantly interrupt the radical chain reactions as compared to those in the absence

337   of scavengers. For instance, the addition of TMP not only scavenge $^3C^*$, but also inhibits

338     $^1O_2$, $O_2^{•-}$, etc. These findings suggest that we cannot directly obtain contributions of

339   each ROS just on basis of the scavenging efficiencies. It should be cautious to apply

340   quenching approach to quantify the role of ROS for pollutant degradation in complex

341   reaction system. Determination of ROS variability during oxidation should be instead

342   by an effective way to elucidate the role of each ROS. Therefore, we tried to detect

343   generated •OH, $O_2^{•-}$ and $^1O_2$ during photochemical reaction using a micro electron spin

344   resonance (ESR) spectrometer (Bruker Magnettech, Berlin, Germany) via DMPO as

345   spin trap to form stable DMPO-•OH or DMPO-$O_2^{•-}$, TEMP to capture $^1O_2$ to produce

346   TEMP-$^1O_2$ spin-adduct (TEMPO). The amounts of radicals can be identified and

347   quantified by the peak patterns in ESR spectra, such as quarter line with a height ratio

348   of 1:2:2:1 for DMPO-•OH, 1:1:1:1 for DMPO-$O_2^{•-}$ and 1:1:1 for TEMP-$^1O_2$ (Guo et al.,

349   2021). Unfortunately, OH radical cannot be detected since the concentrations may not

350   meet the detection limit of the instrument (Fig. S2, ESR spectra of •OH). In contrast,

351   we were able to detect higher concentrations of $^3C^*$ and found intensity of TEMP-$^1O_2$

352   signal reached its maximum at 30 min, then decreased slowly (Fig. S2, ESR spectra of

353     $^1O_2$). Combining the greatest inhibitive effect of TMP with high $^1O_2$ concentration from

ESR method, we can conclude that $^3C^*$ and $^1O_2$ play relatively important roles in eugenol photodegradation.
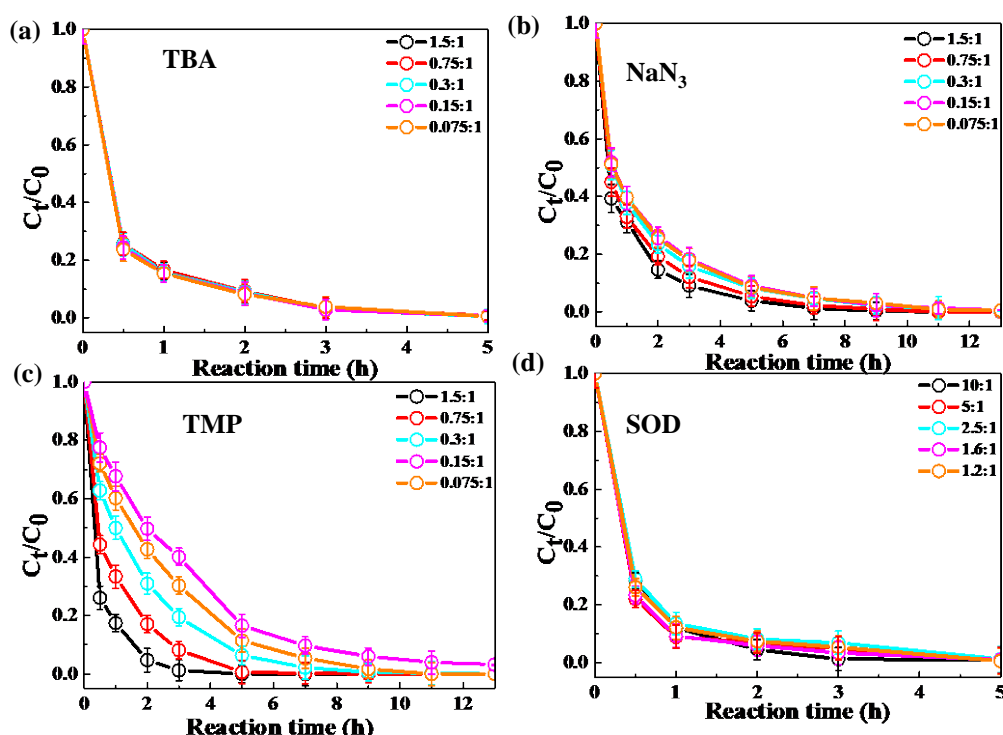
Figure 2. Ratio of residue concentration to initial concentration (C_t/C_0) at different mole ratios as a function of reaction time with (a) TBA quencher, (b) NaN$_3$ quencher, (c) TMP quencher and (d) SOD quencher. Legend represented mole ratios of eugenol to quenchers.

3.2.2 Quenching experiments in OH-initiated photooxidation

To examine the contributions of the quenchers to eugenol degradation for OH-initiated oxidation, TBA and *p*-BQ as trapping agent were added. Similar to $^3C^*$-initiated oxidation, several gradient experiments via varying molar ratios of eugenol to quenchers were conducted. The ratios were set as 6.5:1, 3.2:1, 1.6:1, 1.1:1 and 0.8:1 for *p*-BQ and 3.0:1, 1.5:1, 0.75:1, 0.3:1 and 0.15:1 for TBA. According to Fig. S3, molar ratio only had a slight influence on eugenol degradation, although degradation can be inhibited effectively by quenchers. So, we finally selected appropriated molar ratios of

369   eugenol to quenchers: 0.8 and 0.75 for *p*-BQ and TBA, respectively, since adding too

370   high concentrations of scavengers can actually influence chemical reaction.

371   Variations in the rate constants for above quenching experiments were calculated,

372   respectively, in comparison with tests conducted without quenchers, and the results

373   were listed in Table 1 and presented in Fig. S4. For TBA quenching tests, the rate

374   constant decreased by 18.7% (from 2.73×10^{-4} s^{-1} to 2.22×10^{-4} s^{-1}), showing that •OH

375   radical played a certain role in eugenol photooxidation. Since H_2O_2 was mainly

376   photolyzed at wavelength <300 nm to generate OH radical, but irradiation above 300

377   nm here did not dominate. The *p*-BQ could quench $O_2^{•-}$, which further suppress the

378   generation of other ROS (e.g., •HO_2), as a result, the rate constant decreased the most

379   (from 2.73×10^{-4} s^{-1} to 1.20×10^{-4} s^{-1}), suggesting $O_2^{•-}$ might be responsible for eugenol

380   photodegradation. This hypothesis could be further confirmed by the decline of rate

381   constant under N_2-saturated solution shown later. However, it was difficult to detect

382   both •OH and $O_2^{•-}$ directly due to relatively short half-life and low concentration via

383   ESR in this work.

384   **Table 1.** The reaction rate constants of eugenol in the presence of scavengers. The experimentl

385   conditions were as follows: 0.3 mM eugenol, molar ratios of eugenol to quencher TBA, NaN_3, TMP

386   and SOD, of 1.5, 0.15, 0.075 and 2.5 respectively; mole ratio of eugenol to quencher *p*-BQ and TBA

387   of 0.8 and 0.75 respectively.

$^3C^*$-initiated quenching			
quenchers	ROS	reaction rate constant k (s^{-1})	R^2
no quencher	-	5.75×10^{-4}	0.996
TBA	·OH	2.65×10^{-4}	0.999
SOD	$O_2^{•-}$	2.22×10^{-4}	0.995
NaN_3	$^1O_2$	1.12×10^{-4}	0.999
TMP	$^3C^*$	0.82×10^{-4}	0.999
•OH-initiated quenching			
quenchers	ROS	reaction rate constant k (s^{-1})	R^2
No quencher	-	2.73×10^{-4}	0.995
TBA	·OH	2.22×10^{-4}	0.998

p-BQ	$O_2^{\cdot-}$	1.20×10^{-4}	0.995

388

3.2.3 Influences of different saturated gases

In order to assess the role of O_2 in the mechanism of eugenol photolysis, a few experiments were performed under both O_2-saturated and N_2-saturated instead of air. N_2 gas was purged into reaction solution for ~30 min before experiment to achieve deoxygenated condition. Figure 3 compared the eugenol loss variations and rate constants under three saturated conditions for direct photolysis, OH-initiated and $^3C^*$-initiated oxidation, respectively. The insets of the Fig.3a, 3b and 3c showed the corresponding rate constants. The rate constants under O_2, air and N_2 followed the order of $k_{O_2} > k_{Air} > k_{N_2}$ under both direct photolysis and •OH oxidation, providing evidence in support of O_2 being responsible for eugenol degradation. This might be explained by the fact that O_2 can act as an electron acceptor to generate $O_2^{\cdot-}$ and $•HO_2\cdot$, and subsequently form H_2O_2 and •OH. For direct photolysis, rate constant under O_2-saturated condition increased 14.4% while it decreased 19.3% under N_2 saturation, in contrast to the case of saturated air. For OH-initiated oxidation, the difference of rate constants under three saturated gases became more distinct.

On the contrary, rate constants followed the order of $k_{Air} > k_{N_2} > k_{O_2}$ in $^3C^*$-initiated oxidation system. There are two possible explanations. On the one hand, in N_2-saturated solutions, DMB would be involved in reactions (5-8), followed by more effective generation of $^3DMB^*$. For this reason, eugenol degradation efficiency was higher under N_2 atmosphere than in O_2-saturated solution. On the other hand, in air/O_2 saturated solutions, irradiation of DMB and eugenol would involve reactions (5-12), as a result, the amount of $^3DMB^*$ radical decreased, accompanied by the formation of other

ROS ($^1O_2$, $O_2^{\bullet-}$, •OH, etc) with relatively weak oxidative capacity. In summary, quenching of $^3DMB^*$ by ground state molecular oxygen could account for the lower degradation efficiency in O_2-saturated condition.

$$DMB + h\nu \rightarrow {}^1DMB^* \rightarrow {}^3DMB^* \qquad (5)$$

$$^3DMB^* \rightarrow DMB \qquad (6)$$

$$^3DMB^* \rightarrow Products \qquad (7)$$

$$^3DMB^* + {}^1DMB^* \rightarrow DMB^{\bullet+/\bullet-}(DMB^{\bullet+}+DMB^{\bullet-}) \qquad (8)$$

$$^3DMB^* + O_2 \rightarrow DMB + {}^1O_2 \qquad (9)$$

$$DMB^{\bullet-} + O_2 \rightarrow \cdot DOM^+ + O_2^{\bullet-} \qquad (10)$$

$$O_2^{\bullet-} + 2H^+ \rightarrow H_2O_2 + O_2 \qquad (11)$$

$$H_2O_2 \rightarrow 2\bullet OH \qquad (12)$$
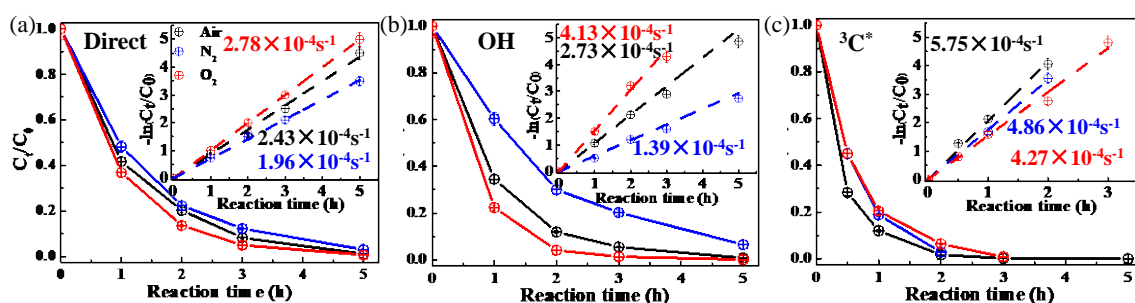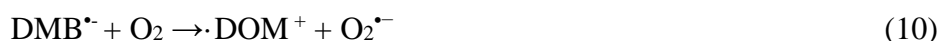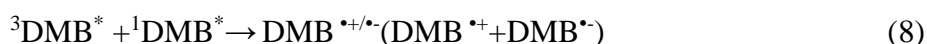
Figure 3. Ratio of remaining concentration to initial concentration (C_t/C_0) as a function of reaction time at different saturated gases under (a) direct photolysis (b) OH-initiated and (c) $^3C^*$-initiated oxidation. Insert plots represented eugenol consumption versus reaction time under different saturated gases: (a) direct photolysis (b) OH-initiated and (c) $^3C^*$-initiated photooxidation.

3.2.4 Variation of pH value and dissolved oxygen

The initial pH values in direct photolysis and OH-initiated oxidation were unadjusted, while initial pH for the $^3C^*$ system was adjusted to 3. The variation of solution pH were presented in Fig.4a. As shown in Fig.4a, solution pH values decreased quickly at the beginning of illumination (from 7.4 to ~5.0 for the first 1h) then tended

432 to smooth in both direct photolysis and OH-initiated oxidation. However, little change

433 of pH value (less than 0.1 unit) was observed for the $^3C^*$-initiated photooxidation, which

434 could be ascribed to very low initial pH value (pH=3). Generally speaking, slight

435 increase of acidity cannot remarkably change pH value when original solution pH was

436 very low. We cannot rule out formation of acid products at $^3C^*$-initiated oxidation. Thus,

437 the decrease of pH value might be related to formation of organic acid and HULIS since

438 carboxylic acids are possibly abundant in HULIS (Huo et al., 2021; Salma et al., 2008).

439 Oxygen can take part in photochemical reaction to form ROS, which may in turn

440 destroy the structure of precursors. In order to further confirm the role of O_2, we

441 measured the oxygen consumption via determining concentration of dissolved oxygen

442 (DO) by a dissolved oxygen meter (Seven2Go Pro S9, Zurich, Switzerland) during the

443 photochemical process. DO was consumed mainly at the first 1 h and kept stable with

444 the reaction time further increasing (Fig.4b-c and Fig.S5). Percentage of DO

445 concentration consumption followed in the order of $^3C^*$>•OH>direct. The maximum

446 DO consumption for $^3C^*$-initiated oxidation process can be explained by the transfer of

447 electrons from $^3C^*$ to O_2 to form $^1O_2$, which was the major contributor to eugenol

448 degradation. Obviously, a steady-state DO level was reached when the consumption

449 rate was equal to the diffusion of O_2 into the solution (Pan et al., 2020).

450 In summary, above experimental results confirmed that O_2 influenced eugenol

451 decomposition and radical conversion via inducing radical chain reactions.

452
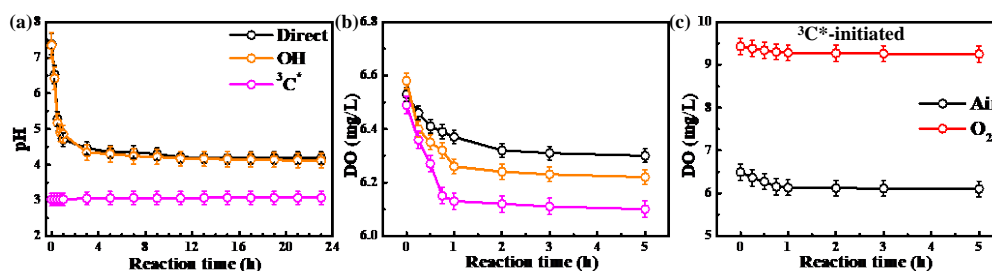
453 **Figure 4.** (a) pH values and (b)-(c) dissolve oxygen as a function of reaction time

454

3.3 Optical properties of products

3.3.1 Light-absorbing properties

UV-vis light spectra at different reaction time are presented in Fig. 5. According to UV-vis spectrum, the wavelength of significant light absorption by eugenol ranges from 260 nm to 300 nm ($n \rightarrow \pi^*$ electronic transitions, 270-350 nm), which in part in the field (280 and 500 nm) of photon fluxes in our lamp. Therefore, we can clearly observe that the characteristic absorption peak at 280 nm of precursor decreased under direct photolysis. As seen in Fig. 5, when adding oxidant H_2O_2, the total variation trend of absorbance was similar to that without oxidant. However, the reaction was extremely quick in the presence of $^3C^*$, and characteristic absorption peak at 280 nm after 3 h irradiation almost disappeared, suggesting nearly complete loss of eugenol, which coincided with the results in Section 3.1 that more than 99% eugenol was degraded at 3 h. Additionally, there is an increase in absorption at longer wavelengths (300-400 nm) over photoreaction, where the original eugenol did not absorb slight, suggesting some light-absorbing products (e.g., brown carbon) appeared. Aqueous photodegradation of some phenolic compounds (e.g., vanillic acid) also observed long-wavelength (300-400nm) absorbance (Tang et al, 2020; Zhao et al., 2015), intensity of which also increased with illumination time. In comparison, there are some differences for light absorbance at wavelength of 300-400 nm in three cases. For direct photolysis and OH-initiated oxidation, light absorbance increased during the first 15 h, then remained at a plateau until 23 h. however, for $^3C^*$-initiated oxidation, light absorbance increased during the first 7 h, then decreased slowly afterwards. The different shapes of UV-vis spectra of photooxidation by •OH and $^3C^*$ might be attributed to different reaction mechanisms, leading to the formation of different products.

The increase of light absorbance at 250 nm ($\pi \rightarrow \pi^*$ electronic transitions) upon

aqueous photo-processing demonstrates the generation of new substances with both the aromatic C=C and carbonyl (C=O) functional groups (Tang et al., 2020). The enhancement at 300-400 nm suggested the probability of HULIS formation because HULIS usually has high molecular weight and conjugated structures. Unfortunately, we did not obtain relative contributions of reaction products to the overall absorbance between 300 to 400 nm because of lack of specific component.
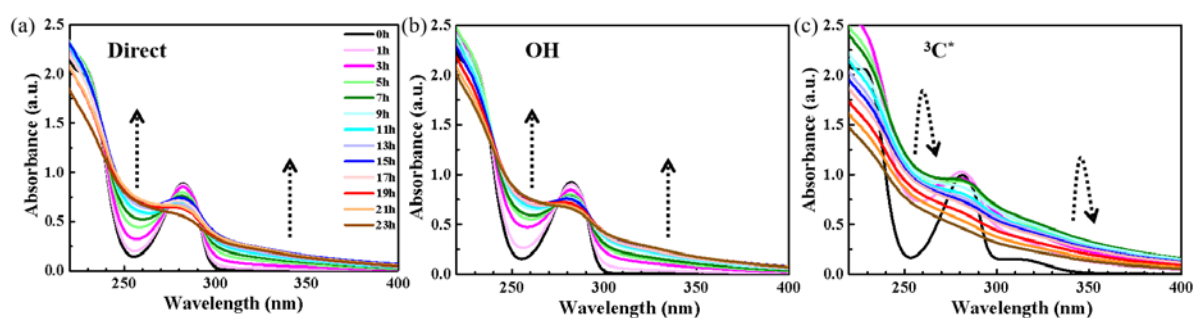
Figure 5. UV–vis light absorption spectra of reacted solutions at different reaction times under (a)direct photolysis, (b)OH-initiated and (c)^{3}C*-initiated photooxidation.

3.3.2 Fluorescence properties

The variation of fluorescence intensities of solutions before (0 h) and upon photolysis (3 h and 7 h) were investigated via the EEM technique, as shown in Fig.6. For comparison, we also presented EEM profiles of pure eugenol (non-irradiated solution), pure DMB, and the end solutions (23 h) of direct photolysis and OH-initiated oxidation (Fig. S6). The peaks at Ex/Em=275/313 nm are ascribed to fluorescence of phenolic structure of parent substance, as suggested by Laurentiis et al. (2013). As shown in both Fig. 6 and Fig. S6, the fluorescence intensity from parent substance decreased after photolysis due to eugenol decay, and the decreasing trend was very fast for ^{3}C*-initiated oxidation. This finding matched with the fast photolysis and large rate constant for ^{3}C*-initiated oxidation. The EEM plots for direct photolysis and OH-

initiated reaction had similar contour patterns as shown in Fig.6 a and b across the entire photochemical reaction, although EEM profile changed significantly with irradiation time. We also observed distinct fluorescent peaks at Ex/Em=235/400-500 nm, indicating that irradiation caused a red shift in fluorescence emission wavelength. As suggested by Chang et al. (2010), fluorophores at Ex/Em=240/400 nm was linked to aromatic structures and condensed saturated bonds including polycyclic aromatic hydrocarbons. Another work (Li et al., 2021) showed that red shift in the fluorescence spectra was usually related to an increase in the size of the ring system and an increase in the degree of conjugation. Previous studies (Chen et al., 2016a; Chen et al., 2019; Laurentiis et al., 2013; Wu et al., 2019) have reported that fluorescent compounds with emission wavelength at 400-500 nm may be highly oxygenated species such as HULIS. Additionally, HULIS have two typical fluorescent peaks in EEM plots at Ex/Em=200-300/400-500nm and Ex/Em=350/400-500nm with higher intensity for the former (Graber and Rudich, 2006; Laurentiis et al., 2013; Vione et al., 2019; Wu et al., 2021). There was evidence (Bianco et al., 2014) to suggest that direct photolysis of tyrosine and 4-phenoxyphenol generated HULIS with new fluorescence signals at Ex/Em = 200−250/400−450 nm and 300/400−450 nm. So, we inferred that new peak at Ex/Em=235/400-500 nm here likely attributed to chromophores of HULIS. For the $^3C^*$-initiated reaction, extra fluorescent peaks at Ex/Em=220-300 nm/400-500nm also appeared at the first 1 h (data not shown), but their intensities were much weaker and gradually disappeared upon prolonged photolysis (3 h). Anyway, EEM results were difficult to interpret because of many complicated substances in reaction samples that might contribute to absorption and emission at certain excitation wavelength, and it is hard to distinguish and isolate fluorescent and nonfluorescent constituents via current techniques. However, we can inferred oligomerization reaction likely took place since

oligomers emit fluorescence at approximately 400 nm (Barsotti et al., 2016).

Another interesting finding was that a small fluorescence peak appeared at Ex/Em=300-350/300-350 nm at different reaction stages. Specifically, it appeared earlier for $^3C^*$ oxidation (at 3 h) than other two systems, and the peak seemed to be a bit stronger in the end solutions of direct photolysis and OH oxidation (Fig. S6). EEM fluorescence spectra for HULIS from fog water have peaks at shorter excitation and emission wavelengths than terrestrial fulvic acids, suggesting a lower content of aromatic structures and condensed unsaturated bond systems (Graber and Rudich, 2006). Moreover, as suggested by Leenheer and Croue (2003), fluorescence peak position of the Ex/Em maximum of HULIS with lower molecular weight shifted towards lower wavelengths, thus, we inferred fluorescence peak at Ex/Em=300-350/300-350 nm might be in part attributed to small organic acid. One unexpected phenomenon in the EEM spectra here is the absence of fluorescence at higher excitation wavelengths (>350 nm), which is often observed in aerosol particles (Wu et al., 2021). This could be attributed to different precursor and aqueous reaction mechanisms (Xie et al. 2016).

Note that uncertainties still exist in using EEM fluorescence technique to characterize molecular composition due to lack of standard EEM profile for specific products of aqueous phase oxidation and clearly more studies are needed in future.
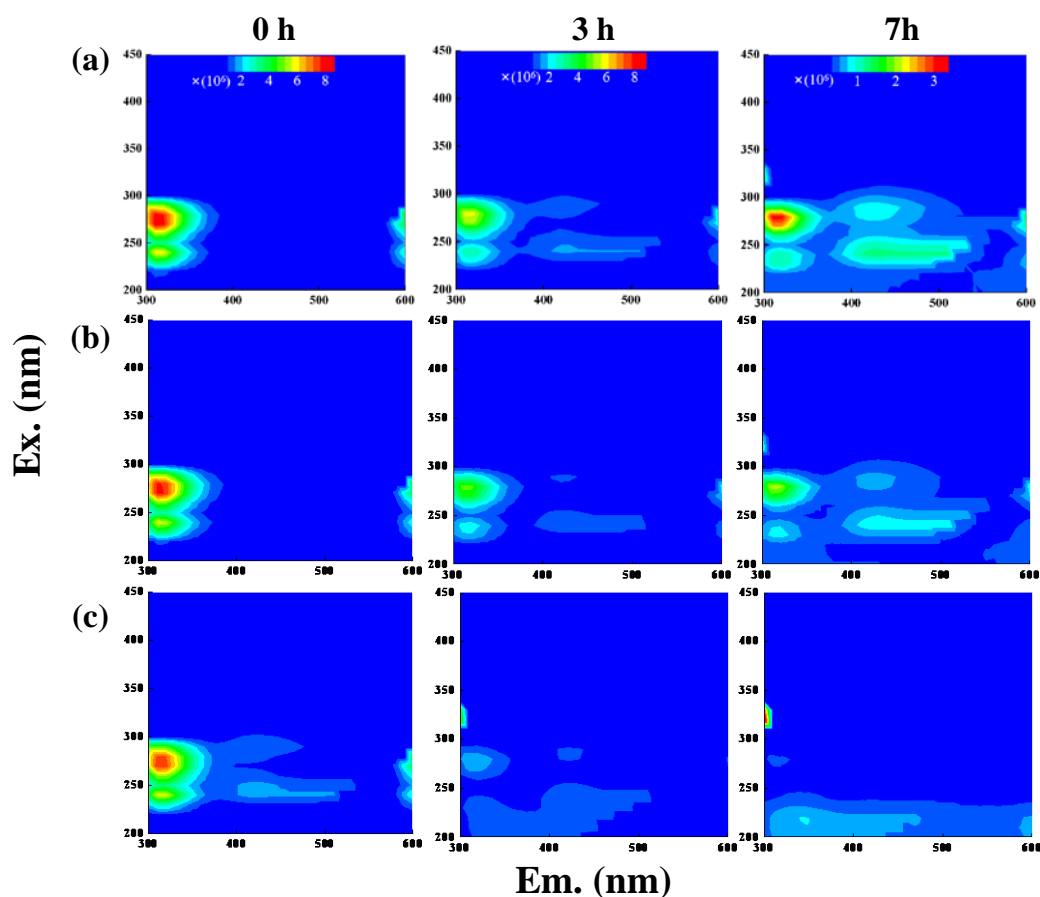
Figure 6. EEM fluorescence spectra of the initial solution (0 h) and those at different reaction time (3 h and 7 h) under (a) direct photolysis, (b) OH-initiated and (c) $^3C^*$-initiated oxidation. The top color bar represents the range of fluorescence intensity.

3.4 HULIS concentration determination

The EEM spectra found new prominent fluorescent peak at Ex/Em=250 nm/400-500 nm, which was likely attributed to chromophores of HULIS. Humic substances are subdivided into fulvic acid (water soluble at all pHs), humic acid (base soluble, acid (pH 1) insoluble) and humin (insoluble at all pHs). In principle, extracted HULIS with polymer-based HLB SPE packing included LMW organic acids, fulvic acids or other humic substances. As suggested by Graber and Rudich (2006), two distinct ranges have been found to characterize humic substances: Ex/Em=330–350/420–480 nm (fulvic-

like), and Ex/Em=250–260/380–480nm (humic-like). So, we inferred most HULIS in this paper was humic-like substance rather than fulvic-like substance. However, EEM technique cannot directly distinguish products solely based on the shapes and limited information of the EEM profiles. Here we determined the HULIS concentrations in the oxidized solutions by using the HPLC method.

Figure 7 presented the measured HULIS concentrations as a function of reaction time. The results show clearly that aqueous phase eugenol oxidation can produce HULIS, and the amount increased gradually in the first 7 h, then remained at a similar level (about 30 mg/L) later in the OH-initiated oxidation. For direct photolysis, HULIS concentration increased until 11h and then retained steady at a level around 40 mg/L. For the $^3C^*$ oxidation, HULIS concentration increased to its maximum at 7 h, but it decreased slightly afterwards. The possible reason was that generated HULIS was capable of further taking part in photochemical reactions since it can act as photosensitizers. Study from Smith (2015) suggested different reaction mechanisms between aqueous benzene-diols with $^3C^*$ and OH radical, with $^3C^*$ oxidation producing highe molecular weight products with less fragmentation. Thus, we inferred that more higher molecular weight HULIS were formed at the first stage due to oligomerization and functionalization as suggested by Jiang et al.(2021), which consequently contributed to fluorescence at Ex of 400 nm (Barsotti et al., 2016).

.

576
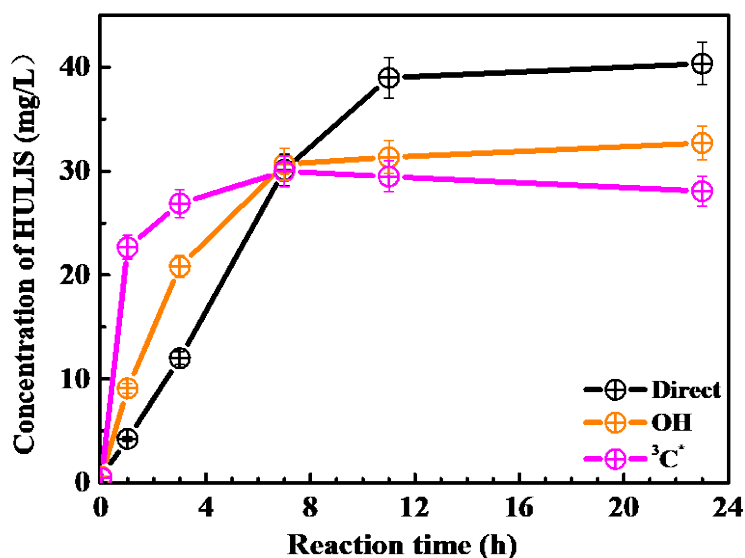
577 **Figure 7.** HULIS concentrations as a function of reaction time for the three systems

578 **3.5 aqSOA mass yield and oxidation degree**

579 **3.5.1 aqSOA mass yield**

580 Figure 8a showed SP-AMS measured organic mass profiles (normalized by sulfate

581 mass, $\Delta Org/SO_4^{2-}$) against the reaction time. As the reaction propagated, $\Delta Org/SO_4^{2-}$

582 increased continuously in $^3C^*$-initiated system. Nevertheless it rise gradually and

583 reached a maximum at 19 h, then remained at a plateau for the direct photolysis and

584 OH-initiated oxidation. Figure 8b illustrated the calculated aqSOA mass yields at

585 different reaction time. The aqSOA mass yields after 1h illumination were in the ranges

586 of 46.2%-196.5%, 22.1%-144.9%, 19.3%-140.1% for oxidation by $^3C^*$, OH radical and

587 direct photolysis, respectively. The SOA mass yield are slightly higher than value

588 (ranging from 80-140%) from phenol-triplet reaction (Ma et al., 2021; Smith et al.,

589 2016; Yu et al., 2014). For the same oxidation time, mass yields from $^3C^*$ oxidation were

590 generally higher than those from OH-initiated oxidation and direct photolysis. These

591 results were similar to investigation on aqueous oxidation of phenolic compounds

592 (Smith et al., 2014, 2015, 2016). There are two plausible reason for high masses for

593 $^3C^*$-initiated oxidation. Firstly, oxidation by $^3C^*$ was more efficiently to form

594 oligomers and functionalized/oxygenated products (Richards-Henderson et al., 2014).

595 Higher oxidative degree of aqSOA from $^3C^*$-initiated photooxidation (see Sec.3.5.2)

596 warrants above hypothesis. Secondly, more light-absorbing products (i.e. HULIS) can

597 participate in SOA formation by acting as photosensitizers (Tsui et al., 2018).

598   The aqSOA mass yields in OH-initiated oxidation of this work agree well with that

599 reported previously for phenolic carbonyls, that is, 120% for syringaldehyde (Huang et

600 al., 2018). Our previous study on eugenol OH oxidation illuminated by a 500 W Xe

601 lamp reported the aqSOA mass yield of ~180% for eugenol (Ye et al., 2020), slightly

602 higher than the value reported here owing to different simulated solar irradiation.

603
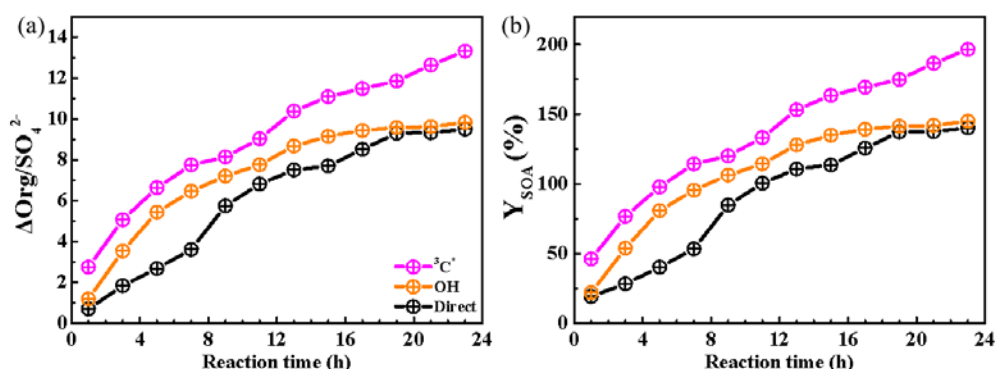
604 **Figure 8.** Variations of the aqSOA mass normalized by sulfate (a) ($\Delta Org/SO_4^{2-}$) and (b) aqSOA mass

605 yields under three conditions.

606 **3.5.2 Oxidation degrees of aqSOA**

607   In order to further represent the oxidation levels of the aqSOA, O/C derived from

608 SP-AMS mass spectrum of the organics was used to assess oxidation degree of aqSOA.

609 In addition, carbon oxidation state (OSc, defined as 2*O/C - H/C) was also calculated

(Kroll et al., 2011). Figure 9a-c described variations of the elemental ratios (O/C and

H/C) and OSc over time. Dramatic increases of O/C and OSc in the initial stage of

oxidation (within 1 hour) were observed, with O/C changed from 0.26 to 0.65, from

0.26 to 0.70, from 0.25 to 0.75, as well as OSc changed from -1.11 to -0.15, from -1.16

to -0.05, from -1.13 to 0.09 for direct photolysis and oxidation by OH and $^3C^*$,

respectively. The O/C was lower than that of other phenolic aqSOA reported (Yu et al.,

2014) due to different substituted group in aromatic ring for precursors. Both O/C and

OSc gradually increased, while H/C decreased for the first 1 h then leveled off. The

enhancements of OSc at 23 h reached 1.22, 1.11 and 0.86 for $^3C^*$-initiated oxidation,

OH-initiated oxidation and direct photolysis, respectively.

Furthermore, the f_{44} vs. f_{43} diagrams (termed as "triangle plot") can be used to

demonstrate the evolution of aqSOA during oxidation (Fig. 9d-f). The f_{44} and f_{43} are

defined as the ratios of signal intensities of m/z 44(CO_2^+) and 43 (mostly $C_2H_3O^+$) to

the total organics. As we known, $CHO2+$ ion in the AMS spectra is an indicator for the

carboxyl functional group (Jiang et al., 2021). Thus, our results that the f_{44} rise

continuously (moved upwards) during $\cdot$OH and $^3C^*$ oxidations, indicating persistent

formation of organic acids, such as formic acid and oxalic acid (Sun et al., 2010).

Concentration of small organic acids rise over photochemical reaction can supported

this assumption (data not shown). Note the f_{44} enhancement was much more significant

for $^3C^*$ oxidation (from 0.07 to 0.16) than direct photolysis (from 0.08 to 0.12) and $\cdot$OH

oxidation (from 0.07 to 0.13), consistent with the behaviors of higher O/C and OSc.

The f_{43} value actually decreased in the first stage (1-3 h) and then increased at the later

stages. The final f_{43} values was almost the same with original solution. As a result, all

data points located outside the f_{44} vs. f_{43} space observed for ambient aerosol AMS

dataset established by Ng et al. (2010), owing to the relatively lower f_{43} values.

635   In summary, our results shown here demonstrate that aqueous phase eugenol

636   photochemical oxidation can generate highly oxygenated products and hence increase

637   the degree of oxygenation of overall SOA.
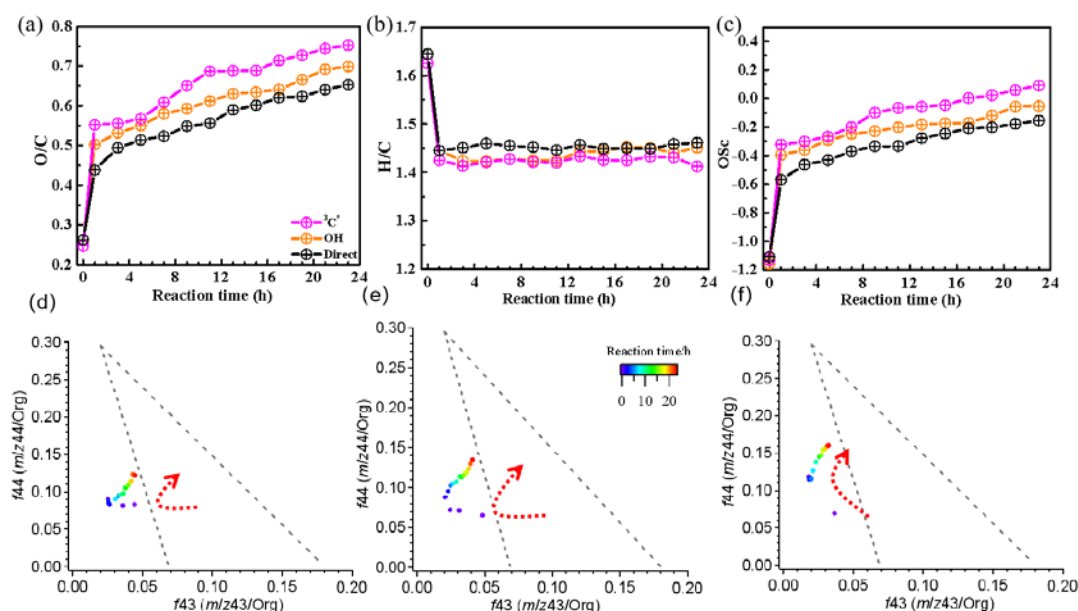
639   **Figure 9.** Variations of elemental ratios (a-c) (H/C, O/C) and OSc as a function of reaction time,

640   and the "Triangle plot" of aqSOA (d-f) under direct photolysis, OH-initiated and $^3C^*$-initiated

641   oxidations.

3.6 Molecular characterization of products and proposed reaction mechanism
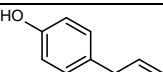
3.6.1 Molecular characterization by GC-MS
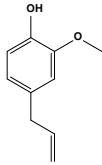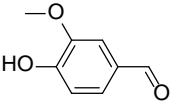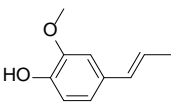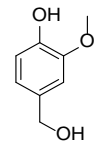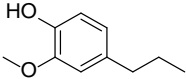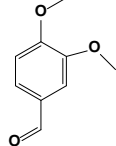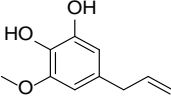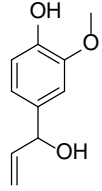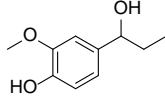
644   SP-AMS was limited to probe bulk composition of low-volatility oxidation

645   products, thus the molecular-level characterization of products was performed by using

646   GC-MS here. The total ion chromatograph (TIC) of GC-MS on the solutions before

647   irradiation (0 h) and at illumination times of 11 and 23 h for the $^3C^*$-initiated

648   photooxidation is shown in Fig. S7. As shown in Fig.S7, eugenol (retention time (RT)

649   at 11.50 min) loss was more than 90% at 11 h, which could be confirmed by the

650   experimental data reported in Section 3.1. Comparison of products at 11 h and 23 h
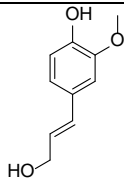
651 showed no significant difference. Similar to aqueous photochemical oxidation from OH

652 oxidant (Ye et al., 2020), a series of products were identified, including two additional

653 compounds, 4-hydroxy-3-methoxy-mandelic acid (MW 198, RT=12.79 min) and 3,4-

654 dihydroxy-, methyl ester-benzoicacid (MW 168, RT=13.39 min). Except for 5-ally-3-

655 methoxybenzene-1,2-diol(MW 180, RT=12.59 min), the other eight products have been

656 detected in both OH and $^{3}C^{*}$-initiated photooxidation. Some of them (Eugenol, DMB,

657 product 1, 2,5) were identified by using certified reference materials, some of them

658 (product 3, 4, 9)identified by matching the NIST database, and others (product 6, 7, 8)

659 were inferred according to the molecular ion peak and fragments from GC-MS,

660 combine with NIST matching results and the start material & reaction conditions.

661   We also found product 1-(4-hydroxy-3-methoxyphenyl) with a carbonyl group

662 was relatively abundant (Fig.S7), suggesting functionalization dominate. In summary,

663 products were mainly from addition/elimination of hydroxyl (-OH), methoxyl ($-OCH_3$)

664 to benzene ring or allyl group and further oxidation to carbonyl or carboxyl compounds..

665 As suggested by Bonin et al.(2007), the OH-addition to the aromatic ring of phenol

666 preferentially takes place at the ortho (48%) and the para (36%) positions, leading to

667 the formation of OH-adduct product 6 (5-allyl-3-methoxybenzene-1,2-diol). Notably,

668 dimers and ring-opening product were not observed, but it cannot be excluded since it

669 would be probably out of the range of GC-MS technique (Vione et al., 2014).

670 **Table 2.** Products identified via GC-MS detection under $^{3}C^{*}$ system

	RT (min)	Material name	Chemical structure	Chemical formula	MW (g/mol)
Product 1	10.68	4-allylphenol		$C_9H_{10}O$	134

Precursor	11.50	Eugenol		$C_{10}H_{12}O_2$	164
Product 2	11.81	4-hydroxy-3-methoxybenzaldehyde		$C_8H_8O_3$	152
Product 3	12.06	(E)-2-methoxy-4-(prop-1-en-1-yl)phenol		$C_{10}H_{12}O_2$	164
Product 4	12.11	4-(hydroxymethyl)-2-methoxyphenol		$C_8H_{10}O_3$	154
Product 5	12.18	2-methoxy-4-propylphenol		$C_{10}H_{14}O_2$	166
Photosensitizer	12.29	3,4-dimethoxybenzaldehyde(DMB)		$C_9H_{10}O_3$	166
Product 6	12.59	5-allyl-3-methoxybenzene-1,2-diol		$C_{10}H_{12}O_3$	180
Product 7	12.65	4-(1-hydroxyallyl)-2-methoxyphenol		$C_{10}H_{12}O_3$	180
Product 8	12.79	4-(1-hydroxypropyl)-2-methoxyphenol		$C_{10}H_{14}O_3$	182

Product 9	12.91	(E)-4-(3-hydroxyprop-1-en-1-yl)-2-methoxyphenol		$C_{10}H_{12}O_3$	180

Note: Precursor (eugenol) and triplet precursor (DMB) was also shown.

3.6.2 Reaction mechanism

The reaction pathways of $^3C*$-initiated photooxidation of eugenol are demonstrated in Scheme 1 based on main products identified by GC-MS. The other intermediates and the potential pathway were inferred and proposed according the identified products and the reaction rationality from start material. To better describe pathways, DMB were expressed as [RCHO] and eugenol as Ph-R for simplicity. First, [RCHO] absorbs light and undergo excitation to $^1[RCHO]^*$, then experiences the intersystem crossing (ISC) to $^3[RCHO]^*$. The $^3[RCHO]^*$ can participate in later reactions via three channels. First, it can react with O_2 to form $^1O_2$ via energy transfer. Secondly, it can become to $[RCHO]^{•-}$, subsequently react with O_2 to generate $O_2^{•-}$ via electron transfer, which can disproportionate to H_2O_2. The decomposition of H_2O_2 can generate OH radical. Thirdly, the $^3[RCHO]^*$ can react with Ph-R to from [Ph-R•] via H-abstraction. The cleavage of [Ph-R•] to free radical segment (such as CH₂CH• or CH₃O•) take place, then an additional hydrogen transfer would happen, resulting in a 2H-addition to the new intermediate to form 4-allyl-phenol (product 1). Similarly, when the CH₂CH• is lost from [Ph-R•], an addition of H_2O would happen on the new compound (product 4) and further oxidized to 4-hydroxy-3-methoxybenzaldehyde (product 2). Another possibility is the intermediate [Ph-R•] could resonate to several different isoelectronic species, the radical position changing to aromatic ring or allyl group site, which would couple with HO• to form hydroxylated eugenol monomer

692 (product 6, 7, 9 MW=180). Consequently, the isoelectronic species at allyl group site

693 could also abstract a hydrogen to form isoeugenol (product 3 MW=164). Also, breakage

694 of C=C into C-C and 2H-addition at allyl group site could form 2-methoxy-4-propyl-

695 phenol (product 5, MW=166). Besides, the C=C breaking intermediate can couple with

696 HO• to form 4-(1-hydroxypropyl)-2-methoxyphenol (product 8, MW=182). In

697 conclusion, $^3C^*$ can directly oxidize eugenol to form SOA or small molecular

698 compounds, or indirectly oxidize eugenol via energy transfer, electron transfer,

699 hydrogen abstraction, proton-coupled electron transfer or other radical chain reactions.

700 The organic groups, such as methoxy, allyl groups can be eliminated from

701 aromatic ring, which then participate in photochemical reaction, resulting in generation

702 of dimers, small organic acids, CO_2 and H_2O, et al. Dimers previously reported from

703 aqueous reaction of 4-methylsyringol with OH were not detected via GC-MS in the

704 present work but dimer fragment ions ($C_{20}H_{22}O_4^+$) were detected by SP-AMS with trace

705 amounts.Functionalization due to the additions of hydroxyl, carbonyl functional groups

706 to the aromatic rings could account for the enhancement of light absorption at

707 wavelength of 300-400 nm. So, aqueous phase reactions of eugenol are likely an

708 important source of BrC in the atmosphere, especially in regions of abundant biomass

709 burning. However, some polar high molecular weight organic acids were not detected

710 due to the limitation of analytical instrument of GC-MS.

711

712

Scheme 1. Proposed eugenol $^3C^*$-initiated reaction mechanism. The red text represents the

compounds listed in Table 1 identified by GC-MS.

3.7 Oxidative potential of products

Previous laboratory studies (Chen et al., 2021; Verma et al., 2015b; Xu et al., 2020) have confirmed that HULIS are major constituents contributing to ROS-generation potential, and HULIS were formed upon aqueous photooxidation of eugenol in this work. Based on above-mentioned results, we want to know whether or not there are

some links between DTT activity and HULIS concentration. So, we detected the OP

variation with reaction time. The OP of aqueous phase products can be represented by

the consumption rate of DTT concentration per minute, defined as R_{DTT}. Figure 10a

shows the DTT consumed mass (M_{DTT}) as a function of incubation times (0, 30, 60, 90,

120 and 150 min) for a triplicate sample (300 µM eugenol) and blank (ultrapure water).

As shown in Figure 10a, M_{DTT} for both blank and eugenol sample were proportional to

incubation time, indicating that ROS-generating substance in reaction solution acts only

as catalyst and was itself not consumed. The slopes represented DTT consumption rates,

which were also illustrated in Fig. 10a. According to Fig. 10a, we obtained average

R_{DTT0} (blank) of 0.31 µM/min and R_{DTT} for initial 300 µM eugenol (before experiment)

of 0.52 µM/min. According to other work, the self-oxidation of DTT might lead to the

consumption of DTT in ultrapure water. Final DTT consumption rate for reaction

solution after photolysis was then blank-corrected by subtracting average R_{DTT0}.

Figure 10b shows changes of blank-corrected R_{DTT} with photolysis time for direct

photolysis, OH-initiated oxidation and $^3C^*$-initiated oxidation, respectively. The R_{DTT}

value of $^3C^*$-initiated oxidation increased quickly and reached the maximum (0.9) at 7

h, then decreased slowly but its end value was slower than that from OH-oxidation. The

R_{DTT} value of OH-oxidation system on the other hand increased slowly and reached the

maximum at 21 h. The R_{DTT} value of direct photolysis system increased continuously

but also slowly to ~0.36 till the termination of oxidation. Nevertheless, we can see that

the R_{DTT} values were higher than that of initial eugenol, providing evidence that

aqueous oxidation products increases oxidative potential, resulting in adverse health

effects than the precursor compounds especially for $^3C^*$-induced photolysis. The DTT

consumption rates are comparable to values by other researchers using the same DTT

method (Charrier and Anastasio, 2012; Lin and Yu, 2019). This finding further indicates

745 the effectiveness of DTT method to represent OP. The unexpected weaker correlation

746 between HULIS concentration and R_{DTT} value implied that oxidative potential was not

747 only dependent with HULIS. Moreover, HULIS with different molecular structure also

748 exhibited different ROS-generation potential (Kramer et al., 2016), as a result, absolute

749 concentration of HULIS did not correlated well with OP.

750
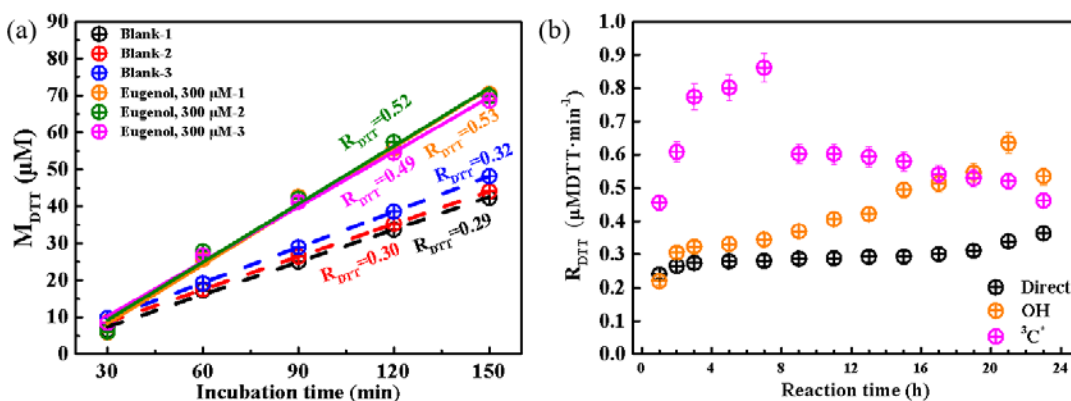
751 **Figure 10.** (a) DTT consumption mass versus incubation time for blanks and 300 μM eugenol in

752 triplicate experiments (b) blank-corrected DTT consumption rate versus reaction time for direct

753 photolysis, OH and $^3C^*$ induced oxidation.

754

4. Conclusions and atmospheric implication

756   This work systematically investigated the aqueous phase photochemistry of eugenol

757 under both OH and $^3C^*$ radicals. Comprehensive analysis of the reaction kinetics,

758 chemical and optical characteristics as well as oxidative potential of the products was

759 conducted. Our results showed eugenol loss more in $^3C^*$-initiated photooxidation. With

760 the combination of quenching experiments, ESR method and different saturated gas

761 experiments, it can be concluded that both $^3C^*$ and $^1O_2$ were responsible for eugenol

762 degradation in $^3C^*$-initiated oxidation, while $O_2^{\bullet-}$ played crucial role in OH-initiated

763 reaction. Interestingly, O_2 can inhibit eugenol degradation by effectively quenching $^3C^*$

radical while it can promote degradation by foster radical chain reactions in OH-induced reaction. Above experimental results also offered us an insight into the degradation mechanism of eugenol involved with ROS. It can also enlighten the readers how to control reaction pathway via regulating the ROS generation during aqueous reaction. Surely, to elucidate the role of each ROS, we should investigate the time-dependent variation of generated ROS via high-sensitivity EPR.

Significant absorption enhancement over the range of near-UV region (300-400 nm) pointed out the continuous generation of BrC (i.e., HULIS). Direct HULIS concentration determination confirmed that HULIS was formed continuously over the course of reaction. Consequently, these light-absorbing products contribute to fluorescence at EX of 400-500 nm. GC-MS analysis confirmed the formation of high molecular weight multi-functional organic compounds, which has also been reported previously in similar aqueous phenolic photochemical experiments (Jiang et al., 2021; Misovich et al., 2021; Tang et al., 2020; Yu et al., 2014). Overall, our work shows that SVOCs-aqSOA is an important source of BrC, therefore aqueous chemical processes may play a role in aerosol light absorption, radiative forcing, as well as climate change. In-depth molecular-level characterization or functional groups with respect to HULIS should be carried out in the future study. Except for influencing the radiative balance of atmosphere, the aqueous photoreaction of phenolic compounds may contribute to the formation of small volatile organics, i.e., dicarboxylic acid, that are emitted in the gas phase and further participate in the SOA formation.

Both DTT consumption rate and EEM have been applied for the investigation of atmospheric aerosol, but not for aqueous-phase photoreaction. Our present work for the first time showed that DTT consumption rate of products was in the order of $^3C^*>OH>$direct, suggesting that oxidative stress of products was higher in $^3C^*$-initiated

789 photolysis process. Additionally, new fluorescence peak at Ex/EM=250/400-500nm in

790 EEM fluorescence spectra suggesting the formation of HULIS. In future, the

791 relationship between EEM components and chemical structure of HULIS must be

792 studied statistically via advanced analysis method. Considering that different chemical

793 species and concentrations of them involved can change reaction pathway leading to

794 different products, optical and toxic investigations of aqueous phase reaction products

795 must be performed under a wide variety of S/IVOCs as precursor.

796   Eugenol emitted in significant quantities by wood combustion undergoes rapid

797 aqueous phase oxidation to produce aqSOA. High-SOA yields (exceed 100%) from

798 aqueous-phase photochemical reactions of eugenol in our work and reported high yields

799 (25-50%) from OH-initiated gas-phase chemistry further demonstrated that phenolic

800 compounds are most significant SOA precursors. Results from highly substituted

801 phenols (has high Henry's law constants) with $^3C^*$ oxidant also showed aqSOA mass

802 yields from triplet reaction was significant under high aerosol liquid water conditions

803 (Ma et al., 2021). Since the highly substituted phenols measured by Schauer et al.(2001)

804 are abundant, together making up roughly 30−45% of total phenols emitted from wood

805 burning, contribution from $^3C^*$-initiated aqueous phase reaction to SOA should be paid

806 more attention. Both OS_C and O/C ratio of aqSOA are higher than those of precursor in

807 this AMS-based study, indicating formation of highly oxidized products (i.e.,

808 carboxylic acid), which also showed the occurrence of oxygenation pathways such as

809 electrophilic addition of OH radical to the aromatic ring. Surely, we should

810 characterized in more detail the molecular-level chemical and light-absorbing

811 components of SOA in order to elucidate the mechanisms responsible for its formation.

812

813 **Data availability.** The data in this study are available from the authors upon request

814 (bess_ye@jsut.edu.cn or caxinra@163.covm)

815 *Supplement.* **The supplement related to this article is available on line at:**

816

817 *Author Contributions:* XDL, YT, LWZ, SSM, SPL, ZZZ and NS conducted the

818 experiments. XDL and YT analyzed the data. XDL and ZLY prepared and wrote the

819 paper with contributions from all co-authors. ZLY and XLG reviewed and commented

820 on the paper.

821 *Competing interests.* The authors declare that they have no conflict of interest.

822

823 *Acknowledgements.* This authors acknowledge support from the National Natural

824 Science Foundation of China (21976093 and 42021004), the Natural Science

825 Foundation of Jiangsu Province (BK20181476), open fund by Jiangsu Key Laboratory

826 of Atmospheric Environment Monitoring and Pollution Control (KHK1904) and the

827 Postgraduate Research & Practice Innovation Program Jiangsu Province

828 (SJCX21_1332, SJCX20_1030) and of Jiangsu University of Technology

829 (XSJCX20_05).

830 *Financial support:* This research was funded by the National Natural Science

831 Foundation of China (21976093 and 42021004), the Natural Science Foundation of

832 Jiangsu Province (BK20181476), and open fund by Jiangsu Key Laboratory of

833 Atmospheric Environment Monitoring and Pollution Control (KHK1904).

834

835 # References

836 Alam, M. S., Delgado-Saborit, J. M., Stark, C., and Harrison, R. M.: Using atmospheric measurements

837   of PAH and quinone compounds at roadside and urban background sites to assess sources and

838   reactivity, Atmos. Environ., 77(3), 24-35, https://doi.org/10.1016/j.atmosenv.2013.04.068, 2013.

839   Alegría, A. E., Ferrer, A., Santiago, G., Sepúlveda, E., and Flores, W.: Photochemistry of water-soluble

840   quinones. Production of the hydroxyl radical, singlet oxygen and the superoxide ion, J.

841   Photochem. Photobiol. Chem., 127, 57-65, https://doi.org/10.1016/S1010-6030(99)00138-0,

842   1999.

843   Arakaki, T., Anastasio, C., Kuroki, Y., Nakajima, H., Okada, K., Kotani, Y., Handa, D., Azechi, S.,

844   Kimura, T., Tsuhako, A., and Miyagi, Y.: A general scavenging rate constant for reaction of

845   hydroxyl radical with organic carbon in atmospheric waters, Environ. Sci. Technol., 47, 8196-

846   8203, https://doi.org/10.1021/es401927b, 2013.

847   Aryal, R., Lee, B. K., Beecham, S., Kandasamy, J., Aryal, N., and Parajuli, K.: Characterisation of road

848   dust organic matter as a function of particle size: A PARAFAC Approach, Water Air Soil Poll.;

849   226, https://doi.org/10.1007/s11270-014-2289-y, 2015.

850   Bari, M, A, Baumbach, G., Kuch, B., and Scheffknecht, G.. Wood smoke as a source of particle-

851   phase organic compoundsin residential areas, Atmos. Environ., 43, 4722-4732,

852   https://doi.org/10.1016/j.atmosenv.2008.09.006, 2009.

853   Barsotti, F., Ghigo, G., and Vione, D. Computational assessment of the fluorescence emission of

854   phenol oligomers: A possible insight into the fluorescence properties of humic-like Substances

855   (HULIS), J. Photochem. Photobio. A, 315, 87-93,

856   https://doi.org/10.1016/j.jphotochem.2015.09.012, 2016.

857   Barzaghi, P. and Herrmann, H.: A mechanistic study of the oxidation of phenol by $OH/NO2/NO_3$ in

858   aqueous solution, Phys. Chem. Chem. Phys., 4, 3669-3675,

859   https://doi.org/10.1039/B201652D, 2002.

860   Bianco, A., Minella, M., De Laurentiis, E., Maurino, V., Minero, C., and Vione, D. Photochemical

861   generation of photoactive compounds with fulvic-like and humic-like fluorescence in aqueous

862   solution, Chemosphere, 111, 529-536, https://dx.doi.org/10.1016/j.chemosphere.2014.04.035,

863   2014.

864   Bonin, J., Janik, I., Janik, D. and Bartels, D. M.: Reaction of the hydroxyl radical with phenol in water

865   up to supercritical conditions, J. Phys. Chem. A, 111(10), 1869-1878,

866   https://doi.org/10.1021/jp0665325, 2007.

867   Canagaratna, M. R., Jimenez, J. L., Kroll, J. H., Chen, Q., Kessler, S. H., Massoli, P., Hildebrandt Ruiz,

868   L., Fortner, E., Williams, L. R., Wilson, K. R., Surratt, J. D., Donahue, N. M., Jayne, J. T., and

Worsnop, D. R.: Elemental ratio measurements of organic compounds using aerosol mass spectrometry: characterization, improved calibration, and implications, Atmos. Chem. Phys., 15, 253-272, https://doi.org/10.5194/acp-15-253-2015, 2015.

Chang, J. L., and Thompson, J. E.: Characterization of colored products formed during irradiation of aqueous solutions containing H_2O_2 and phenolic compounds, Atmos. Environ., 44, 541-551, https://doi.org/10.1016/j.atmosenv.2009.10.042, 2010.

Charrier, J. G., and Anastasio, C.: On dithiothreitol (DTT) as a measure of oxidative potential for ambient particles: evidence for the importance of soluble transition metals, Atmos. Chem. Phys. 12, 9321-9333, https://doi.org/10.5194/acp-12-9321-2012, 2012.

Chen, Q., Ikemori, F., and Mochida, M.: Light Absorption and excitation-emission fluorescence of urban organic aerosol components and their relationship to chemical structure, Environ. Sci. Technol., 50, 10859-10868, https://doi.org/10.1021/acs.est.6b02541, 2016a.

Chen, Q., Miyazaki, Y., Kawamura, K., Matsumoto, K., Coburn, S., Volkamer, R., Iwamoto, Y., Kagami, S., Deng, Y., Ogawa, S., Ramasamy, S., Kato, S., Ida, A., Kajii, Y., and Mochida, M.: Characterization of chromophoric water-soluble organic matter in urban, forest, and marine aerosols by HR-ToF-AMS analysis and excitation-emission matrix spectroscopy, Environ. Sci. Technol., 50, 10351-10360, https://doi.org/10.1021/acs.est.6b01643, 2016b.

Chen, Q., Wang, M., Wang, Y., Zhang, L., Li, Y., and Han, Y.: Oxidative potential of water-soluble matter associated with chromophoric substances in $PM_{2.5}$ over Xi'an, China, Environ. Sci. Technol., 53, 8574-8584, https://doi.org/10.1021/acs.est.9b01976, 2019.

Chen, Y., Li, N., Li, X., Tao, Y., Luo, S., Zhao, Z., Ma, S., Huang, H., Chen, Y., Ye, Z., and Ge, X.: Secondary organic aerosol formation from $^3C^*$-initiated oxidation of 4-ethylguaiacol in atmospheric aqueous-phase, Sci. Total. Environ., 723, 137953, https://doi.org/10.1016/j.scitotenv.2020.137953, 2020.

Cho, A. K., Sioutas, C., Miguel, A. H., Kumagai, Y., Schmitz, D. A., Singh, M., Eiguren-Fernandez, A., and Froines, J. R.: Redox activity of airborne particulate matter at different sites in the Los Angeles Basin, Environ. Res., 99, 40-7, https://doi.org/10.1016/j.envres.2005.01.003, 2005.

De Laurentiis, E., Sur, B., Pazzi, M., Maurino, V., Minero, C., Mailhot, G., Brigante, M., and Vione, D.: Phenol transformation and dimerisation, photosensitised by the triplet state of 1-nitronaphthalene: A possible pathway to humic-like substances (HULIS) in atmospheric waters,

899   Atmos. Environ., 70, 318-327, https://doi.org/10.1016/j.atmosenv.2013.01.014, 2013.

900   Dou, J., Lin, P., Kuang, B. Y., and Yu, J.: Reactive oxygen species production mediated by humic-like

901   substances in atmospheric aerosols: enhancement effects by pyridine, imidazole, and their

902   derivatives, Environ. Sci. Technol., 49(11), 6457-6465, https://doi.org/10.1021/es5059378,

903   2015.

904   Ervens, B., Turpin, B. J., and Weber, R. J.: Secondary organic aerosol formation in cloud droplets and

905   aqueous particles (aqSOA): a review of laboratory, field and model studies, Atmos. Chem. Phys.,

906   11, 11069-11102, https://doi.org/10.5194/acp-11-11069-2011, 2011.

907   Fang, T., Verma, V., Bates, J. T., Abrams, J., Klein, M., Strickland, M. J., Sarnat, S. E., Chang, H. H.,

908   Mulholland, J. A., Tolbert, P. E., Russell, A. G., and Weber, R. J.: Oxidative potential of ambient

909   water-soluble $PM_{2.5}$ in the southeastern United States: contrasts in sources and health

910   associations between ascorbic acid (AA) and dithiothreitol (DTT) assays, Atmos. Chem. Phys.,

911   16, 3865-3879, https://doi.org/10.5194/acp-16-3865-2016, 2016.

912   Faust, J. A., Wong, J. P., Lee, A. K., and Abbatt, J. P.: Role of aerosol liquid water in secondary organic

913   aerosol formation from volatile organic compounds, Environ. Sci. Technol., 51, 1405-1413,

914   https://doi.org/10.1021/acs.est.6b04700, 2017.

915   Graber, E. R., and Rudich, Y.: Atmospheric HULIS: how humic-like are they? A comprehensive and

916   critical review, Atmos. Chem. Phys., 6, 729-753, https://doi.org/10.5194/acp-6-729-2006,

917   2006.

918   George, K. M., Ruthenburg, T. C., Smith, J., Yu, L., Zhang, Q., Anastasio, C., and Dillner, A. M.: FT-IR

919   quantification of the carbonyl functional group in aqueous-phase secondary organic aerosol from

920   phenols, Atmos. Environ., 100, 230-237, https://doi.org/10.1016/j.atmosenv.2014.11.011, 2015.

921   Gilardoni, S., Massoli, P., Paglione, M., Giulianelli, L., Carbone, C., Rinaldi, M., Decesari, S., Sandrini,

922   S., Costabile, F., Gobbi, G. P., Pietrogrande, M. C., Visentin, M., Scotto, F., Fuzzi, S., and

923   Facchini, M. C.: Direct observation of aqueous secondary organic aerosol from biomass-

924   burning emissions, Proc. Natl. Acad. Sci. USA., 113, 10013-8,

925   https://doi.org/10.1073/pnas.1602212113, 2016.

926   Gligorovski, S., Strekowski, R., Barbati, S., and Vinoe, D.: Environmental implications of hydroxyl

927   radicals (OH), Chem. Rev., 115(24), 13051-13092, https://doi.org/10.1021/cr500310b, 2015.

928   Guo, Y., Zhang, Y., Yu, G., and Wang, Y., Revisiting the role of reactive oxygen species for pollutant

929   abatement during catalytic ozonation: the probe approach versus the scavenger approach, Appl.

930   Catal. B Environ., 280, 119418, https://doi.org/10.1016/j.apcatb.2020.119418, 2021.

931 Hawthorne, S.B., Krieger M.S., Miller D.J., and Mathiason M.B. Collection and quantitation of

932   methoxylated phenol tracers for atmospheric pollution from residential wood stoves, Environ. Sci.

933   Technol., 23,470-475, https://doi.org/10.1021/es00181a013, 1989.

934 He, L., Schaefer, T., Otto, T., Kroflic, A., and Herrmann, H.: Kinetic and theoretical study of the

935   atmospheric aqueous-phase reactions of OH radicals with methoxyphenolic compounds, J. Phys.

936   Chem. A, 123, 7828-7838, https://doi.org/10.1021/acs.jpca.9b05696, 2019.

937 Herrmann, H.: Kinetics of aqueous phase reaction relevant for atmospheric chemistry, Chem. Rev., 103,

938   4691-4716, https://doi.org/10.1021/cr020658q, 2003.

939 Herrmann, H., Schaefer, T., Tilgner, A., Styler, S. A., Weller, C., Teich, M. and Otto, T.: Tropospheric

940   aqueous-phase chemistry: kinetics, mechanisms, and its coupling to a changing gas phase,

941   Chem. Rev., 115(10), 4259-4334, https://doi.org/10.1021/cr500447k, 2015.

942 Hong, J., Han, B., Yuan, N., and Gu, J.: The roles of active species in photo-decomposition of organic

943   compounds by microwave powered electrodeless discharge lamps, J. Environ. Sci. (China), 33,

944   60-8, https://doi.org/10.1016/j.jes.2014.12.016, 2015.

945 Huang, D., Zhang, X., Chen, Z. M., Zhao, Y., and Shen, X. L.: The kinetics and mechanism of an aqueous

946   phase isoprene reaction with hydroxyl radical, Atmos. Chem. Phys., 11, 7399-7415,

947   https://doi.org/10.5194/acp-11-7399-2011, 2011.

948 Huang, D., Zhang, Q., Cheung, H. H. Y., Yu, L., Zhou, S., Anastasio, C., Smith, J. D., and Chan, C. K.:

949   Formation and evolution of aqSOA from aqueous-phase reactions of phenolic carbonyls:

950   comparison between ammonium sulfate and ammonium nitrate solutions, Environ. Sci.

951   Technol., 52, 9215-9224, https://doi.org/10.1021/acs.est.8b03441, 2018.

952 Huo, Y., Guo, Z., Li, Q., Wu, D., Ding, X., Liu, A., Huang, D., Qiu, G., Wu, M., Zhao, Z., Sun, H., Song,

953   W., Li, X., Chen, Y., Wu, T., and Chen, J. Chemical fingerprinting of HULIS in particulate

954   matters emitted from residential coal and biomass combustion, Environ. Sci. Technol., 55, 3593-

955   3603. https://doi.org/10.1021/acs. est.0c08518, 2021.

956 Jiang, W., Misovich, M. V., Hettiyadura, A. P. S., Laskin, A., McFall, A. S., Anastasio, C., and Zhang, Q.:

957   Photosensitized reactions of a phenolic carbonyl from wood combustion in the aqueous phase-

958   chemical evolution and light absorption properties of aqSOA, Environ. Sci. Technol., 55, 5199-

959   5211, https://doi.org/10.1021/acs.est.0c07581, 2021.

960 Kaur, R., and Anastasio, C.: First measurements of organic triplet excited states in atmospheric waters,

961   Environ. Sci. Technol., 52, 5218-5226, https://doi.org/10.1021/acs.est.7b06699, 2018.

962 Kaur, R., Labins, J. R., Helbock, S. S., Jiang, W., Bein, K. J., Zhang, Q., and Anastasio, C.: Photooxidants

963   from brown carbon and other chromophores in illuminated particle extracts, Atmos. Chem.

964   Phys., 19, 6579-6594, https://doi.org/10.5194/acp-19-6579-2019, 2019.

965 Kramer, A.J., Rattanavaraha, W., Zhang, Z., Gold, A., Surratt, J.D., and Lin, Y.-H. Assessing the oxidative

966   potential of isoprene-derived epoxides and secondary organic aerosol, Atmos. Environ., 130,

967   211-218, https://dx.doi.org/10.1016/j.atmosenv.2015.10.018, 2016.

968 Kroll, J. H., Donahue, N. M., Jimenez, J. L., Kessler, S. H., Canagaratna, M. R., Wilson, K. R., Altieri,

969   K. E., Mazzoleni, L. R., Wozniak, A. S., Bluhm, H., Mysak, E. R., Smith, J. D., Kolb, C. E., and

970   Worsnop, D. R.: Carbon oxidation state as a metric for describing the chemistry of atmospheric

971   organic aerosol, Nat. Chem., 3, 133-9, https://doi.org/10.1038/nchem.948, 2011.

972 Laurentiis, E. D., Socorro, J., Vione, D., Quivet, E., Brigante, M., Mailhot, G., Wortham, H., and

973   Gligorovski, S.: Phototransformation of 4-phenoxyphenol sensitised by 4-

974   carboxybenzophenone: evidence of new photochemical pathways in the bulk aqueous phase and

975   on the surface of aerosol deliquescent particles, Atmos. Environ., 8, 569-578,

976   https://doi.org/10.1016/j.atmosenv.2013.09.036, 2013.

977 Lee, A. K. Y., Hayden, K. L., Herckes, P., Leaitch, W. R., Liggio, J., Macdonald, A. M., and Abbatt, J. P.

978   D.: Characterization of aerosol and cloud water at a mountain site during WACS 2010: secondary

979   organic aerosol formation through oxidative cloud processing, Atmos. Chem. Phys., 12, 7103-7116,

980   https://doi.org/10.5194/acp-12-7103-2012, 2012.

981 Leenheer, J. A., and Croue, J. P. Characterizing aquatic dissolved organic matter, Environ. Sci.

982   Technol., 37, 18A-26A, https://doi.org/10.1021/es032333c, 2003.

983 Li, F., Tsona, N. T., Li, J., and Du, L.: Aqueous-phase oxidation of syringic acid emitted from biomass

984   burning: formation of light-absorbing compounds, Sci. Total Environ., 765, 144239,

985   https://doi.org/10.1016/j.scitotenv.2020.144239, 2021.

986 Li, Y. J., Huang, D. D., Cheung, H. Y., Lee, A. K. Y., and Chan, C. K.: Aqueous-phase photochemical

987   oxidation and direct photolysis of vanillin-a model compound of methoxy phenols from biomass

988   burning, Atmos. Chem. Phys., 14, 2871-2885, https://doi.org/10.5194/acp-14-2871-2014, 2014.

Lim, Y. B., Tan, Y., Perri, M. J., Seitzinger, S. P., and Turpin, B. J.: Aqueous chemistry and its role in secondary organic aerosol (SOA) formation, Atmos. Chem. Phys., 10, 10521-10539, https://doi.org/10.5194/acpd-10-14161-2010, 2010.

Lin, M., and Yu, J. Z.: Dithiothreitol (DTT) concentration effect and its implications on the applicability of DTT assay to evaluate the oxidative potential of atmospheric aerosol samples, Environ. Pollut., 251, 938-944, https://doi.org/10.1016/j.envpol.2019.05.074, 2019.

Liu, C.G., Liu, Y.C., Chen, T.Z., Liu, J., and He, H. Rate constant and secondary organic aerosol formation from the gas-phase reaction of eugenol with hydroxyl radicals, Atmos. Chem. Phys., 19, 2001-2013, https://doi.org/10.5194/acp-19-2001-2019, 2019.

Ma, L., Guzman, C., Niedek, C., Tran, T., Zhang, Q. and Anastasio, C.: Kinetics and mass yields of aqueous secondary organic aerosol from highly substituted phenols reacting with a triplet excited state, Environ. Sci. Technol., 55(9), 5772-5781, doi:10.1021/acs.est.1c00575, 2021.

Ma, Y., Cheng, Y., Qiu, X., Cao, G., Kuang, B., Yu, J.Z., and Hu, D. Optical properties, source apportionment and redox activity of Humic-Like Substances (HULIS) in airborne fine particulates in Hong Kong, Environ. Pollut., 255,113087, https://doi.org/10.1016/j.envpol.2019.113087, 2019.

Mabato, B. R. G., Lyu, Y., Ji, Y., Li, Y., Huang, D., Li, X., Nah, T., Lam, C. H., and Chan, C. K.: Aqueous secondary organic aerosol formation from the direct photosensitized oxidation of vanillin in the absence and presence of ammonium nitrate, Atmos. Chem. Phys., 22, 273-293, https://doi.org/10.5194/acp-22-273-2022, 2022.

McWhinney, R. D., Zhou, S., and Abbatt, J. P. D.: Naphthalene SOA: redox activity and naphthoquinone gas–particle partitioning, Atmos. Chem. Phys., 13, 9731-9744, https://doi.org/10.5194/acp-13-9731-2013, 2013.

Misovich, M. V., Hettiyadura, A. P. S., Jiang, W. Q., and Zhang, Q. Molecular-level study of the photo-oxidation of aqueous-phase guaiacyl acetone in the presence of ^{3}C*: formation of brown carbon products, ACS Earth Space Chem., 5, 1983-1996, https://doi.org/10.1021/acsearthspacechem.1c00103, 2021.

Mladenov, N, Alados-Arboledas, L., Olmo, F .J., Lyamani, H., Delgado, A., Molina, A., and Reche, I.: Applications of optical spectroscopy and stable isotope analyses to organic aerosol source discrimination in an urban area, Atmos. Environ., 45, 1960-1969, https://doi.org/

1019   10.1016/j.atmosenv.2011.01.029, 2011.

1020   Nau, W. M., and Scaiano, J. C.: Oxygen quenching of excited aliphatic ketones and diketones, J. Phys.

1021   Chem., 100, 11360-11367, https://doi.org/10.1021/jp960932i, 1996.

1022   Ng, N. L., Canagaratna, M. R., Zhang, Q., Jimenez, J. L., Tian, J., Ulbrich, I. M., Kroll, J. H., Docherty,

1023   K. S., Chhabra, P. S., Bahreini, R., Murphy, S. M., Seinfeld, J. H., Hildebrandt, L., Donahue, N.

1024   M., DeCarlo, P. F., Lanz, V. A., Prevot, A. S. H., Dinar, E., Rudich, Y., and Worsnop, D. R.:

1025   Organic aerosol components observed in Northern Hemispheric datasets from aerosol mass

1026   spectrometry, Atmos. Chem. Phys., 10, 4625-4641, https://doi.org/10.5194/acp-10-4625-2010,

1027   2010.

1028   Pan, Y., Ma, H., Li, Z., Du, Y., Liu, Y., Yang, J., and Li, G.: Selective conversion of lignin model veratryl

1029   alcohol by photosynthetic pigment via photo-generated reactive oxygen species, Chem. Eng. J,

1030   393, 124772, https://doi.org/10.1016/j.cej.2020.124772, 2020.

1031   Raja, P., Bozzi, A., Mansilla, H., and Kiwi, J.: Evidence for superoxide-radical anion, singlet oxygen and

1032   OH-radical intervention during the degradation of the lignin model compound (3-methoxy-4-

1033   hydroxyphenylmethylcarbinol), J. Photochem. Photobiol. Chem., 169, 271-278,

1034   https://doi.org/10.1016/j.jphotochem.2004.07.009, 2005.

1035   Richards-Henderson, N. K., Hansel, A. K., Valsaraj, K. T., and Anastasio, C. Aqueous oxidation of green

1036   leaf volatiles by hydroxyl radical as a source of SOA: Kinetics and SOA yields, Atmos. Environ.,

1037   95, 105-112, http://dx.doi.org/10.1016/j.atmosenv.2014.06.026, 2014.

1038   Rossignol, S., Aregahegn, K. Z., Tinel, L., Fine, L., Nozière, B., and George, C.: Glyoxal induced

1039   atmospheric photosensitized chemistry leading to organic aerosol growth, Environ. Sci.

1040   Technol., 48, 3218-3227, https://doi.org/10.1021/es405581g, 2014.

1041   Scharko, N. K., Berke, A. E., and Raff, J. D.: Release of nitrous acid and nitrogen dioxide from nitrate

1042   photolysis in acidic aqueous solutions, Environ. Sci. Technol., 48, 11991-2001,

1043   https://doi.org/10.1021/es503088x, 2014.

1044   Salma, I., and Láng, G. G. How many carboxyl groups does an average molecule of humic-like

1045   substances contain? Atmos. Chem. Phys., 8, 5997-6002, https://doi.org/10.5194/acpd-8-10005-

1046   2008, 2008.

1047   Schauer, J. J., Kleeman, M. J., Cass, G. R., and Simoneit, B. R. Measurement of emissions from air

1048   pollution sources. 3. C1-C29 organic compounds from fireplace combustion of wood,

1049   Environ. Sci. Technol., 35, 1716-1728, https://doi.org/10.1021/es001331e, 2001.

1050   Simpson, C.D., Paulsen, M., Dills, R. L., Liu, L.-J.S., and Kalman, A.A. Determination of

1051   methoxyphenols in ambient atmospheric particulate matter: Tracers for wood combustion,

1052   Environ. Sci. Technol., 39, 631-637, https://doi.org/10.1021/es0486871, 2005.

1053   Smith, J. D., Kinney, H., and Anastasio, C.: Aqueous benzene-diols react with an organic triplet excited

1054   state and hydroxyl radical to form secondary organic aerosol. Phys. Chem. Chem. Phys., 17,

1055   10227, https://doi.10.1039/c4cp06095d, 2015.

1056   Smith, J. D., Kinney, H, and Anastasio, C. Phenolic carbonyls undergo rapid aqueous photodegradation

1057   to form low-volatility, light-absorbing products, Atmos. Environ., 126, 36-44,

1058   https://doi.org/10.1016/j.atmosenv.2015.11.035, 2016.

1059   Smith, J. D., Sio, V., Yu, L., Zhang, Q., and Anastasio, C.: Secondary organic aerosol production from

1060   aqueous reactions of atmospheric phenols with an organic triplet excited state, Environ. Sci.

1061   Technol., 48, 1049-1057, https://doi.org/10.1021/es4045715, 2014.

1062   Sun, Y., Zhang, Q., Anastasio, C., and Sun, J.: Insights into secondary organic aerosol formed via

1063   aqueous-phase reactions of phenolic compounds based on high resolution mass spectrometry,

1064   Atmos. Chem. Phys., 10, 4809–4822, https://doi.org/10.5194/acp-10-4809-2010, 2010.

1065   Tang, S., Li, F., Tsona, N.T., Lu, C., Wang, X., and Du, L.: Aqueous-phase photooxidation of vanillic

1066   acid: a potential source of humic-like substances (HULIS), ACS Earth Space Chem., 4, 862-

1067   872, https://doi.org/10.1021/acsearthspacechem.0c00070, 2020.

1068   Tsui, W. G., and McNeill, V. F. Modeling secondary organic aerosol production from photosensitized

1069   humic-like substances (HULIS), Environ. Sci. Technol. Lett., 5, 255-259.

1070   https://doi.org/10.1021/acs.estlett.8b00101, 2018.

1071   Verma, V., Fang, T., Xu, L., Peltier, R. E., Russell, A. G., Ng, N. L., and Weber, R. J.: Organic aerosols

1072   associated with the generation of reactive oxygen species (ROS) by water-soluble $PM_{2.5}$,

1073   Environ. Sci. Technol., 49, 4646-56, https://doi.org/10.1021/es505577w, 2015a.

1074   Verma, V., Wang, Y., El-Afifi, R., Fang, T., Rowland, J., Russell, A.G., and Weber, R. J.: Fractionating

1075   ambient humic-like substances (HULIS) for their reactive oxygen species activity-assessing the

1076   importance of quinones and atmospheric aging, Atmos. Environ., 120, 351-359,

1077   https://doi.org/10.1016/j.atmosenv.2015.09.010, 2015b.

1078   Vione, D., Albinet, A., Barsotti, F., Mekic, M., Jiang, B., Minero, C., Brigante, M., and Gligorovski, S.:

1079   Formation of substances with humic-like fluorescence properties, upon photoinduced

1080   oligomerization of typical phenolic compounds emitted by biomass burning, Atmos. Environ.,

1081   206, 197-207, https://doi.org/10.1016/j.atmosenv.2019.03.005, 2019.

1082   Vione, D., Maurino, V., Minero, C., Pelizzetti, E., Harrison, M. A., Olariu, R. I., and Arsene, C.:

1083   Photochemical reactions in the tropospheric aqueous phase and on particulate matter, Chem.

1084   Soc. Rev., 35, 441-53, https://doi.org/10.1039/b510796m, 2006.

1085   Vione, D., Maurino, V., and Minero, C.: Photosensitised humic-like substances (HULIS) formation

1086   processes of atmospheric significance: a review, Environ. Sci. Pollut. Res., 21, 11614-11622,

1087   https://doi.org/10.1007/s11356-013-2319-0, 2014.

1088   Wang, J., and Wang, S. Reactive species in advanced oxidation processes: Formation, identification and

1089   reaction mechanism, Chem. Eng.J., 401, 126158, https://doi.org/10.1016/j.cej.2020.126158,

1090   2020.

1091   Wang, L., Lan, X., Peng, W., and Wang, Z.: Uncertainty and misinterpretation over identification,

1092   quantification and transformation of reactive species generated in catalytic oxidation processes:

1093   A review, J Hazard. Mater., 408, 124436, https://doi.org/10.1016/j.jhazmat.2020.124436, 2021.

1094   Wu, G., Ram, K., Fu, P., Wang, W., Zhang, Y., Liu, X., Stone, E. A., Pradhan, B. B., Dangol, P. M.,

1095   Panday, A., Wan, X., Bai, Z., Kang, S., Zhang, Q., and Cong, Z.: Water-soluble brown carbon

1096   in atmospheric aerosols from Godavari (Nepal), a regional representative of south Asia, Environ.

1097   Sci. Technol., 53, 3471-3479, https://doi.org/10.1021/acs.est.9b00596, 2019.

1098   Xie, M., Mladenov, N., Williams, M. W., Neff, J. C., Wasswa, J., and Hannigan, M. P.: Water soluble

1099   organic aerosols in the Colorado Rocky Mountains, USA: composition, sources and optical

1100   properties, Sci. Rep., 6, https://doi.org/10.1038/srep39339, 2016.

1101   Xu, X., Lu, X., Li, X., Liu, Y., Wang, X., Chen, H., Chen, J., Yang, X., Fu, T., Zhao, Q., and Fu, Q. ROS-

1102   generation potential of Humic-like substances (HULIS) in ambient $PM_{2.5}$ in urban Shanghai:

1103   Association with HULIS concentration and light absorbance, Chemosphere, 256, 127050,

1104   https://doi.org/10.1016/j.chemosphere.2020.127050 0045-6535, 2020.

1105   Yang, J., Au, W. C., Law, H., Lam, C. H., and Nah, T.: Formation and evolution of brown carbon during

1106   aqueous-phase nitrate-mediated photooxidation of guaiacol and 5-nitroguaiacol, Atmos.

1107   Environ., 254, 118401, https://doi.org/10.1016/j.atmosenv.2021.118401, 2021.

1108   Ye, Z., Zhuang, Y., Chen, Y., Zhao, Z., Ma, S., Huang, H., Chen, Y., and Ge, X.: Aqueous-phase oxidation

1109   of three phenolic compounds by hydroxyl radical: Insight into secondary organic aerosol

1110   formation yields, mechanisms, products and optical properties, Atmos. Environ., 223, 117240,

1111   https://doi.org/10.1016/j.atmosenv.2019.117240, 2020.

1112 Yu, L., Smith, J., Laskin, A., Anastasio, C., Laskin, J., and Zhang, Q.: Chemical characterization of SOA

1113   formed from aqueous-phase reactions of phenols with the triplet excited state of carbonyl and

1114   hydroxyl radical, Atmos. Chem. Phys., 14, 13801–13816, https://doi.org/10.5194/acp-14-

1115   13801-2014, 2014.

1116 Yu, L., Smith, J., Laskin, A., George, K. M., Anastasio, C., Laskin, J., Dillner, A. M., and Zhang, Q.:

1117   Molecular transformations of phenolic SOA during photochemical aging in the aqueous phase:

1118   competition among oligomerization, functionalization, and fragmentation, Atmos. Chem. Phys.,

1119   16, 4511-4527, https://doi.org/10.5194/acp-16-4511-2016, 2016.

1120 Zhang, T., Huang, S., Wang, D., Sun, J., Zhang, Q., Xu, H., Ho, S., Cao, J., and Shen, Z. Seasonal and

1121   diurnal variation of $PM_{2.5}$ HULIS over Xi'an in Northwest China: Optical properties, chemical

1122   functional group, and relationship with reactive oxygen species (ROS), Atmos. Environ., 268,

1123   118782, https://doi.org/10.1016/j.atmosenv.2021.118782, 2022.

1124 Zhang, X., Chen, Z. M., and Zhao, Y.: Laboratory simulation for the aqueous OH-oxidation of methyl

1125   vinyl ketone and methacrolein: significance to the in-cloud SOA production, Atmos. Chem.

1126   Phys., 10, 9551-9561, https://doi.org/10.5194/acp-10-9551-2010, 2010.

1127 Zhao, R., Lee, A. K., and Abbatt, J. P.: Investigation of aqueous-phase photooxidation of glyoxal and

1128   methylglyoxal by aerosol chemical ionization mass spectrometry: observation of

1129   hydroxyhydroperoxide formation, J. Phys. Chem. A., 116, 6253-63,

1130   https://doi.org/10.1021/jp211528d, 2012.

1131 Zhao, R., Mungall, E. L., Lee, A. K. Y., Aljawhary, D., and Abbatt, J. P. D.: Aqueous-phase

1132   photooxidation of levoglucosan-a mechanistic study using aerosol time of flight chemical

1133   ionization mass spectrometry (Aerosol ToF-CIMS), Atmos. Chem. Phys., 14, 9695-9706,

1134   https://doi.org/10.5194/acpd-14-8819-2014, 2014.

1135 Zhao, R., Lee, A.K.Y., Huang, L., Li, X., Yang, F., and Abbat, J.P.D.Photochemical processing of aqueous

1136   atmospheric brown carbon, Atmos. Chem. Phys., 15, 6087-6100, https://doi.org/10.5194/acpd-

1137   15-2957-2015, 2015.

1138 Zhou, Z., Chen, B., Qu, X., Fu, H., and Zhu, D.: Dissolved black carbon as an efficient sensitizer in the

1139   photochemical transformation of 17#-estradiol in aqueous solution, Environ. Sci. Technol., 52,

1140   10391-10399, https://doi.org/10.1021/acs.est.8b01928, 2018.